J. Fluid Mech. (1999), *vol.* 379, *pp.* 71–104. Printed in the United Kingdom

Large-eddy simulations of a round jet in crossflow

By LESTER L. YUAN, ROBERT L. STREET AND JOEL H. FERZIGER†

Environmental Fluid Mechanics Laboratory, Department of Civil and Environmental Engineering, Stanford University, Stanford, CA 94305-4020, USA

(Received 22 September 1997 and in revised form 4 August 1998)

This paper reports on a series of large-eddy simulations of a round jet issuing normally into a crossflow. Simulations were performed at two jet-to-crossflow velocity ratios, 2.0 and 3.3, and two Reynolds numbers, 1050 and 2100, based on crossflow velocity and jet diameter. Mean and turbulent statistics computed from the simulations match experimental measurements reasonably well. Large-scale coherent structures observed in experimental flow visualizations are reproduced by the simulations, and the mechanisms by which these structures form are described. The effects of coherent structures upon the evolution of mean velocities, resolved Reynolds stresses, and turbulent kinetic energy along the centreplane are discussed. In this paper, the ubiquitous far-field counter-rotating vortex pair is shown to originate from a pair of quasi-steady 'hanging' vortices. These vortices form in the skewed mixing layer that develops between jet and crossflow fluid on the lateral edges of the jet. Axial flow through the hanging vortex transports vortical fluid from the near-wall boundary layer of the incoming pipe flow to the back side of the jet. There, the hanging vortex encounters an adverse pressure gradient and breaks down. As this breakdown occurs, the vortex diameter expands dramatically, and a weak counter-rotating vortex pair is formed that is aligned with the jet trajectory.

1. Introduction

The jet in crossflow (JICF) is a highly complex turbulent flow, with applications in a vast array of engineering problems. The basic case of a non-buoyant turbulent jet issuing normally into a flat plate boundary layer provides an excellent model for applications ranging from understanding pollutant dispersion from smokestacks to designing V/STOL airplanes. Experimental and numerical investigations of the flow physics of the jet in crossflow have been quite plentiful, and we can only cite a small selection of the literature here. For readers who would like more coverage, Margason (1993) conducts a more thorough review of jet in crossflow research.

Early experimental work, such as performed by Pratte & Baines (1967) centred around measuring the jet trajectory for different combinations of flow parameters. Later research began focusing on collecting mean velocity data and turbulence statistics. Ramsey & Goldstein (1970) and Crabb, Durao & Whitelaw (1981) were some of the first to use hot wires and laser-Doppler anemometry to measure mean and fluctuating velocity magnitudes in the jet. More thorough measurements were later

† Also: Department of Mechanical Engineering, Stanford University, Stanford, CA 94305-3030, USA.

taken by Andreopoulos & Rodi (1984), who used a triple wire probe to simultaneously measure all three components of velocity. Sherif & Pletcher (1989) performed similar measurements, but used hot films in a water tunnel, so they were able to use significantly lower Reynolds numbers.

As with many other turbulent flows, coherent structures dominate the behaviour of the JICF, and interpreting turbulent statistics requires some understanding of the evolution of these structures. The most important of these features is arguably the counter-rotating vortex pair (CVP), which is often observed in the farfield aligned with the trajectory of the jet. This flow structure has been documented repeatedly in a variety of experiments, and its presence seems to contribute to many of the distinctive characteristics of the jet. Its origins, however, are still the subject of much debate. Andreopoulos (1985), Sykes, Lewellen & Parker (1986), Coehlo & Hunt (1989), and many others have proposed mechanisms by which the CVP is generated. All of the authors seem to agree that the original source of the vorticity is the jet shear layer, but the means by which this vorticity realigns to produce the CVP is still unclear. In visualizing the generation of the vortex pair from the azimuthally-oriented vorticity in the jet shear layer, most researchers model the jet as a series of vortex rings. Vorticity on the lateral edges of each vortex ring is then correctly oriented to create a CVP. Mechanisms proposed by each author differ, however, when explaining how consecutive vortex rings coalesce into two line vortices. Andreopoulos (1985) hypothesises that the downstream edge of each vortex ring is compressed by the mean strain, which eliminates the spanwise vorticity and leaves the CVP. Sykes *et al.* (1986) propose a mechanism by which the upstream edge of one vortex ring is cancelled through an interaction with the downstream edge of the following ring. Coehlo & Hunt (1989) suggest that the reorganization of jet shear layer vorticity caused by entrained crossflow fluid initiates the development of the CVP. To date, though, no definitive mechanism for the formation of the CVP has achieved widespread acceptance.

Recent advances in experimental flow visualization techniques have provided the means for researchers to probe the flow and identify other large-scale features. Fric & Roshko (1994) use smoke illuminated by a laser sheet to examine the vortical structure in the wake of the jet. They find vertically oriented vortices which connect the jet body with the wall boundary layer. Their studies reveal that these vortices arise from separation events of the wall boundary layer as it sweeps around the edge of the jet. Kelso & Smits (1995) use a hydrogen bubble technique to examine the horseshoe vortices which appear upstream of the jet exit. These vortices form when the wall boundary layer encounters an adverse pressure gradient at the front of the jet and separates. They find a connection between the oscillations in the horseshoe vortices and oscillations in the wake behind the jet. Haven (1996) performs extensive flow visualization and velocity measurements above the jet exit. She proposes that lateral edge vorticity in the incoming pipe flow is tilted by a gradients in the vertical velocity profile. The tilted vorticity then rolls up into streamwise vortices that form the CVP. Kelso, Lim & Perry (1996) employ dye tracers in a water tunnel and flying hot wires in a wind tunnel to shed further light upon the nature of the jet structure. They postulate that the initial vortical roll-up of the jet shear layer initiates the downstream development of the CVP through a vortex breakdown mechanism.

Numerical simulations can provide a useful source of new data for turbulent flows, as simulations allow examination of quantities which are difficult to measure accurately in experiments. Up until very recently, the only feasible means of numerically simulating this flow has been through solving the Reynolds-averaged Navier–Stokes

equations. Sykes *et al.* (1986) solved them using a version of the Mellor Yamada 2.5 turbulence model. They used a very limited number of points and did not resolve the flow near the bottom wall, which limits the value of their results. Claus & Vanka (1992) used a simple k–ϵ turbulence model with many more points and still had trouble reproducing mean experimental results. They concluded from their study that Reynolds-averaged Navier–Stokes models developed for use with simple boundary layer flows were not accurate enough for the complexities of the jet in crossflow. Kim & Benson (1992) attempted to improve on the turbulence model by introducing turbulent time scales which vary in the flow. They also employed a numerical method which allowed them to simulate the flow beneath the flat plate, greatly improving the inflow boundary condition for the jet. Their results reproduced mean flow statistics reasonably well, but severely underpredicted turbulent kinetic energy. Demuren (1993) modelled the full Reynolds stress transport equations in his simulations, but still failed to accurately reproduce mean velocities and overpredicted turbulent kinetic energy.

The advent of faster computers with larger core memories has allowed researchers to contemplate time-accurate simulations of the flow. Rudman (1994) performed a simulation of the JICF that resolved the temporal evolution of the flow. However, he did not resolve all scales of motion and did not use a subgrid-scale model, which affected the quantitative accuracy of his results. He did generate qualitative temporal results which shed some light into the evolution of large-scale structures in the flow. Jones & Wille (1996) performed a large-eddy simulation using a dynamic turbulence model. However, they used approximate boundary conditions at the wall rather than resolving the turbulent wall boundary layer, which introduced inaccuracies in their computed results that are difficult to evaluate.

While recent experiments have shed much new light upon the effects of large-scale structures in the JICF, many questions remain unanswered. Numerical simulations can provide more complete information about the velocity field, but most simulations to date have been unable to accurately reproduce the flow. In this paper we report on large-eddy simulations that we have performed of the JICF in which we have achieved quantitative agreement with experimental measurements. The main focus of this paper is to examine the development of large-scale features in the flow and to understand how these features affect turbulent statistics. We will discuss other characteristics of the flow, such as scalar transport, entrainment, and the jet trajectory, in subsequent papers.

The rest of this paper is organized as follows. We discuss the equations which govern the behaviour of this flow and the numerical method we use to solve these equations in §2. In §3 we present the computational domain used to represent the flow and discuss the boundary conditions which have been applied. We then compare simulation results with experimental measurements in §4 and discuss reasons for the observed discrepancies. Section 5 is devoted to examining the coherent vortical structures observed in the flow and comparing them to experimental observations. We present turbulent statistics in §6 and draw final conclusions in §7.

2. Governing equations and numerical method

The governing equations are the grid-filtered, incompressible Navier–Stokes equations:

$$\frac{\partial \overline{u}_k}{\partial x_k} = 0, \tag{2.1a}$$

$$\frac{\partial \overline{u}_i}{\partial t} + \frac{\partial}{\partial x_j}(\overline{u}_j \overline{u}_i) = -\frac{\partial \overline{p}}{\partial x_i} + \frac{1}{Re_D}\frac{\partial^2 \overline{u}_i}{\partial x_j^2} - \frac{\partial}{\partial x_j}\tau_{ij}, \tag{2.1b}$$

where summation over the three coordinate directions is implied in terms with repeated indices, and a line over a variable indicates a grid-filtered quantity; u_i are the Cartesian velocity components non-dimensionalized by the crossflow velocity U_∞, and p is the pressure divided by the density and non-dimensionalized by U_∞^2. The spatial coordinates have all been non-dimensionalized by the initial jet diameter, D. Thus, the appropriate Reynolds number for this flow is defined as $Re_D = U_\infty D/\nu$, where ν, the kinematic viscosity of the fluid, is assumed to be constant over the flow conditions of the simulations.

The effects of velocities not resolved by the computational grid are included by means of a subgrid-scale stress, which is defined as

$$\tau_{ij} = \overline{u_i u_j} - \overline{u}_i \overline{u}_j; \tag{2.2}$$

τ_{ij} is modelled in these simulations using the dynamic subgrid-scale model described in Zang, Street & Koseff (1993), in which the model coefficient is determined locally from the velocity field which has been filtered on two different levels. This model has been shown to be effective in transitionally turbulent flows and to have the capacity to predict the backscatter of energy from the subgrid scales to the resolved flow. The model is also stable with only local averaging of the model coefficient. Thus, it is ideally suited to this flow, which has no homogeneous directions and contains both laminar and turbulent regions.

The governing equations are transformed into a generalized coordinate system and discretized using a control volume formulation. The fractional step, non-staggered solution technique of Zang, Street & Koseff (1994) is then used to solve the equations. This technique uses two sets of variables, defining Cartesian velocities and pressures at cell centres, and contravariant volume fluxes at cell faces. This 'co-located' variable layout combines the low metric storage requirements of a non-staggered grid layout with the pressure convergence qualities of a staggered grid layout. The solution is advanced in time using a semi-implicit scheme that is formally second-order accurate. All spatial discretizations are also second-order accurate.

The code has been validated extensively against standard test cases, reproducing both analytical solutions to the Navier–Stokes equations and experimentally measured flows fields (see Zang *et al.* 1994). This code has been used to simulate a variety of laboratory-scale flows ranging from free surface turbulent channel flows to upwelling flows, some of which have been documented in Salvetti *et al.* (1997) and Zang & Street (1995*a*). Formal grid resolution studies were conducted in these simpler flows, and in general, these studies found that while some minor quantitative changes occur as the grids are refined, the code reproduces the same qualitative features as long as the large-scale structures are sufficiently resolved. Because the simulations run for this study require significant amounts of computer time, formal grid resolution studies are impractical. Instead, we have followed the guidance provided by previous simulations in selecting the number and spacing of grid points and in resolving key features, such as boundary and shear layers. Then, based on the previous grid resolution studies using this code, it follows that qualitative features are realistically reproduced by the simulations, and that quantitative results are reasonable.

The physical geometry of the JICF problem consists of a circular hole extending a short distance below a flat plate. Forcing a single grid to conform to both the plate and the hole would be extremely difficult, so we divide the computational

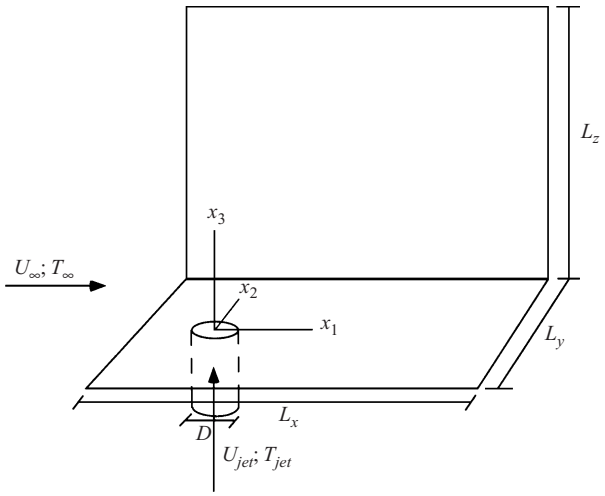

FIGURE 1. Flow configuration schematic (dimensional).

domain into several subdomains, using cylindrically shaped grids near the round hole and rectangular grids in the main domain. The algorithms used in this domain decomposition are based on the techniques of Zang & Street (1995 *b*). In the current set of simulations, we use a total of thirteen grids as described in Yuan (1997) (see also Yuan & Street 1996), which allows us to efficiently resolve the circular boundary condition of the jet exit and the flow through the main channel.

3. Flow configuration

The flow configuration we use in our simulations is that of an idealized jet in crossflow (JICF). The jet begins as a turbulent pipe flow which then issues into a flat-plate boundary layer through an orifice which is flush with the plane of the flat plate (figure 1). The coordinate system we use is also depicted in figure 1, with the origin located at plate level and in the centre of the orifice. Here, x_1 represents distance in the streamwise direction, x_2 the spanwise direction, and x_3 the vertical. In this paper, the coordinate system (x, y, z), which corresponds directly with (x_1, x_2, x_3), will also be used. In this alternative coordinate system, (u, v, w) represent velocities in each of the three directions.

The dimensions of the main section vary slightly depending upon the jet-to-crossflow velocity ratio, R. For the higher R results presented in this paper, the size of the domain is $12.7D$ in the streamwise direction, $8.0D$ in the spanwise, and $12.0D$ in the vertical. For the lower R cases, the jet penetrates less deeply into the crossflow, so the vertical extent of the domain can be reduced. The computational domain is therefore $13.7D \times 8.0D \times 9.0D$. In all cases, the centre of the jet is $2.7D$ downstream of the crossflow inlet plane.

Domain decomposition provides a convenient technique for placing fine grids in optimal locations. A total of 1.34×10^6 control volumes is used to discretize the domain, of which approximately 45% are placed directly downstream of the jet exit. Individual grids are also refined as they approach solid surfaces, so the first control volume next to the jet exit has dimensions of $\Delta x = 0.004D$ and $\Delta z = 0.006D$. If we scale these dimensions by the shear velocity of the incoming turbulent pipe flow, we find $\Delta x^+ = 1.4$ and $\Delta z^+ = 2.2$. This fine resolution is consistent with the limiting behaviour of the subgrid-scale model, ensuring that virtually all scales of the fluid

motion are resolved and that the subgrid-scale contributions to the turbulent stresses are negligible near solid surfaces.

The flow in the main section is driven by fixing the inflow velocity profile as a laminar boundary layer profile, with an initial boundary layer height of $0.5D$ and free-stream velocity of U_∞, matching the experimental conditions listed by Sherif & Pletcher (1989). On the lateral and top surfaces, free-slip boundary conditions are prescribed, while on the bottom, a no-slip boundary condition is enforced. The inlet plane, lateral walls, and upper wall were all placed at distances that were judged to be sufficient to prevent the imposed boundary conditions from artificially constraining the solution. Subsequent inspection of velocity profiles between these boundaries and the region of interest confirmed the initial assumption, as the effects of the jet do not appear in the velocity profiles until well into the computational domain.

We have evaluated a variety of possible outflow conditions, including recently proposed schemes by Jin & Braza (1993) and Johansson (1993). However, we have found that the outflow condition which best combines simplicity of implementation with good performance is simply a zero gradient condition for all flow variables. The more complex boundary conditions added computational cost and did not appreciably improve results.

The incoming pipe velocity profile is prescribed in the pipe a distance of $1.0D$ below the flat plate, allowing the flow to develop naturally as the jet emerges into the crossflow. To provide a realistic turbulent pipe flow at the inflow boundary, we simultaneously ran a second simulation of a temporally-evolving pipe flow and extracted instantaneous velocity profiles at each time step. These profiles were then used as velocity boundary conditions at the pipe inflow for the JICF simulation. The appropriate Reynolds number for the pipe flow simulation was determined beforehand through an iterative process, such that the volume flux supplied by the pipe matched that required by the JICF simulation. For the high Re_D simulations, the temporal pipe flow simulation was run at $Re_\tau = 380$, while the low Re_D simulations required $Re_\tau = 211$. Re_τ is the Reynolds number based on the shear velocity of the incoming turbulent pipe flow.

Stability constraints are quite restrictive in these simulations, as the high jet velocity flows normal to very fine grids. Consequently, the time steps used in the simulations are quite small, and each simulation requires a significant amount of computer time. Approximately 2000 hours are required for each simulation when run on a single processor of a Cray J90, and approximately a quarter the time is required when run on a single processor of a Cray C90. This computation time corresponds to approximately $80T_u$, where the time scale is defined as $T_u = D/U_\infty$.

4. Comparisons to experiment

We compare the numerical results to the experimental measurements of Sherif & Pletcher (1989, hereafter referred to as SP) who recorded measurements for a JICF with a moderate Re_D. Numerical values for our simulation parameters are compared with those used in the experiment in table 1. As can be seen from the table, Re_D in the experiment is approximately twice the magnitude of the largest simulation Re_D, and the values of R used in Cases 3I and 3II are approximately 18 % less than those used in SP. We discuss the reasons for these choices in parameter values in subsequent sections.

SP only used a single hot-film probe to measure velocity on the centreplane. Consequently, they only provide vertical profiles of velocity magnitude and fluctuations.

	R	Re_D
Case 2I	2.0	2100
Case 3I	3.3	1050
Case 3II	3.3	2100
Sherif & Pletcher (1989)	4.0	4820

TABLE 1. Simulation and experimental parameters.

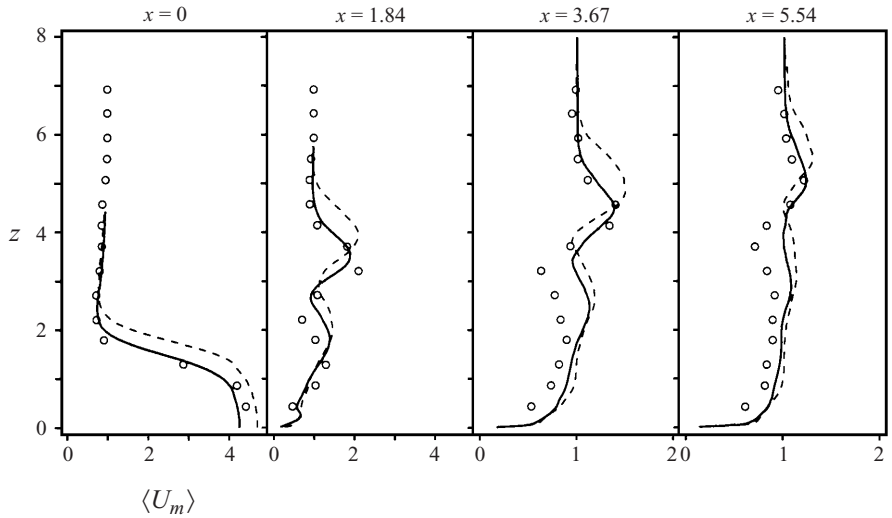

FIGURE 2. Vertical profiles of mean velocity magnitude at the centreplane. Solid line, Case 3II; dashed line, Case 3I; open circles, SP.

We compute the same quantities on the centreplane from our data using the following equations:

$$\left.\begin{aligned} U_m &= (u_1^2 + u_2^2 + u_3^2)^{1/2}, \\ u_m'' &= U_m - \langle U_m \rangle, \\ u_{rms} &= \langle u_m''^2 \rangle^{1/2}, \end{aligned}\right\} \tag{4.1}$$

where $\langle\,\rangle$ denotes a long time average. At this point we also drop the cumbersome overline notation, and the variable, u_i, now represents only the non-dimensional, grid-filtered, resolved velocities. In figure 2, we have plotted vertical profiles of velocity magnitude on the centreplane at four streamwise locations for Cases 3I and 3II. (Notice that the horizontal scale changes for the last two plots.) The data of SP at the same locations are plotted as symbols on the same graphs. The agreement between simulation and experimental results is quite good. The simulations reproduce the two local maxima observed in the experiment in each downstream profile and correctly predict the evolution of the velocity profile. Quantitatively, the locations of the local maxima predicted in Case 3I are too high. Case 3II matches the experimental measurements more closely in the placement of the maximum magnitude in each vertical profile, although the maximum magnitude is slightly underpredicted at $x = 1.84$. We speculate on the cause of this strong dependence on Re_D in the context of coherent structures in §5.1. Overall, each Case 3II profile seems to match experiment closely above the point of maximum velocity; but, below this point, the computed velocity magnitudes are consistently higher than experiment.

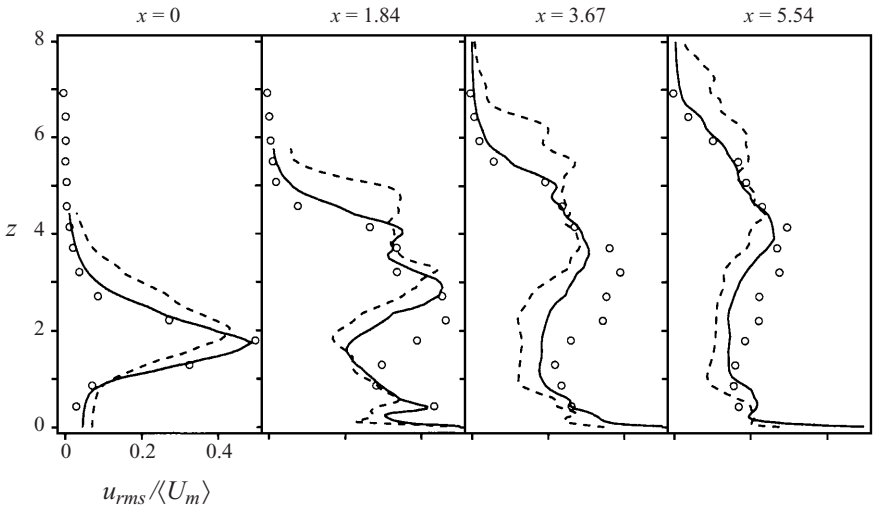

FIGURE 3. Vertical profiles of r.m.s. fluctuations in velocity magnitude. Solid line, Case 3II; dashed line, Case 3I; open circles, SP.

In figure 3 we plot the r.m.s. fluctuations of velocity magnitude defined in (4.1) for Cases 3I and 3II with the experimental measurements of SP. The trends observed in the mean velocity are valid here. Case 3I profiles rise too rapidly, while Case 3II profiles compare quite well with experiment. At the first station, directly over the jet exit, the agreement between Case 3II and experiment is excellent. At subsequent stations downstream, computed profiles agree well with experiment in the upper half of the profile, but underpredict r.m.s. magnitudes in the lower half. Because we follow SP and normalize r.m.s. values by the local mean velocity, some of this underprediction may stem from the high mean velocities we observed in figure 2. However, the high mean velocities do not fully explain the discrepancies we observe.

The vertical locations of the maximum r.m.s. intensities seem to occur just below the vertical location of maximum mean velocity, where the gradients in the velocity magnitude are high. Very near the wall, mean velocities approach zero, so the scaled r.m.s. fluctuations become very large. Directly above this, a second peak in the vertical profiles can be detected. This peak corresponds to the fluctuations generated by the wall wake vortices. Some of the experimental measurements hint at this behaviour (for example, at $x = 1.84$), but in general, the measurements were not taken sufficiently close to the wall to capture the trend.

Two main discrepancies occur in the comparisons between computed results and experimental measurements. Velocities are consistently higher than experiment in the lower regions of the vertical profiles, and to achieve comparable rise heights, the simulation velocity ratio must be smaller than that used in experiment. We believe these discrepancies occur for two reasons. First, the jet inflow conditions of the experiments differ from the idealized inflow conditions of the simulations. Secondly the lower Re_D of the simulations results in a fundamentally different crossflow wall boundary layer.

4.1. *Jet inflow conditions*

The development of the downstream flow is particularly sensitive to the characteristics of the inflow jet. In addition to the main production runs, we have performed several

	R	Re_D	Flow condition
Case A	4.0	1050	Plug flow
Case B	4.0	1050	Mean turbulent pipe profile
Case C	4.0	1050	Temporally-evolving pipe
Case 3I	3.3	1050	Temporally-evolving pipe
Case 3II	3.3	2100	Temporally-evolving pipe

TABLE 2. Inflow profile specifications.

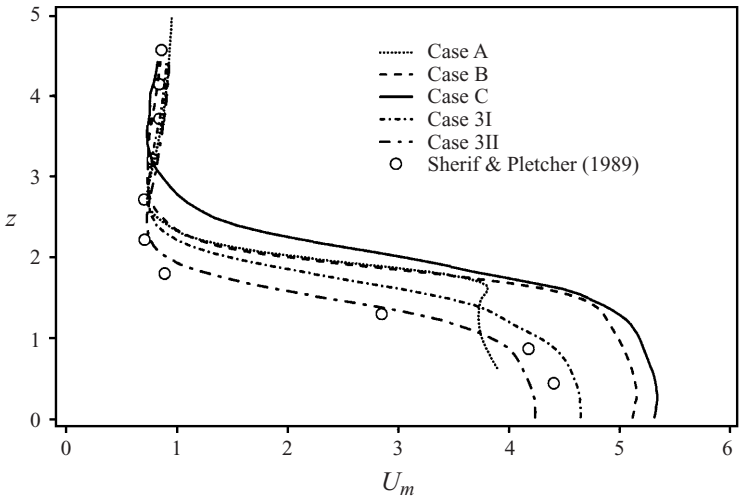

FIGURE 4. Effect of jet inflow conditions. See text for descriptions of cases. Lines, computed results; open circles, SP.

short simulations to examine the effects of different types of inflow conditions. In these test simulations, denoted Cases A, B and C, we varied Re_D, the velocity ratio, and the flow condition (listed in detail in table 2). One other difference of note is that in Case A the inflow condition was specified at the level of the flat plate, while in all subsequent cases the profile was specified $1.0D$ below the plate. The timescale of the turbulence near the jet exit is short relative to that farther downstream, so the convergence of the time-averaged velocity profiles near the jet exit is relatively rapid. Thus, the computational expense of these test cases was somewhat smaller than the production runs.

The resulting velocity magnitude profiles over the jet exit for each case are shown in figure 4. The run conditions of Case A differ the most from the experimental parameters, and consequently produce the worst results. At about $z = 1.7$ we observe an odd shoulder in the profile before it drops off toward the jet outlet. The strange shape of the profile results from prescribing the inflow boundary condition at the surface of the flat plate, which forces horizontal velocities to zero at the inflow and constrains the flow in an unphysical manner.

In Case B, we moved the location of the inflow plane below the flat plate and specified a steady mean turbulent pipe profile, using a standard 1/7 law approximation to the pipe flow. This velocity profile is rounder than the plug flow of Case A, and so, to achieve the same bulk velocity, the centreline velocity of Case B is substantially higher. This high centreline velocity is evident in the high velocity magnitude at $z = 0$.

Moving the inflow location below the plane of the flat plate corrected the general shape of the profile, but the jet still rises too quickly, and the slope of the velocity profile is too flat.

In all subsequent cases (C, 3I, and 3II) data from a temporally-evolving pipe simulation were used as the inflow boundary condition. The improvement is obvious. The slope of the profile is greater in the high shear region, matching the experimental measurements and indicating that the jet turns more gradually into the crossflow. However, Case C still overshoots the experimental data substantially.

In Cases 3I and 3II, we reduced the velocity ratio from 4.0 to 3.3 because the data of SP showed a slight discrepancy. They quote a pipe Reynolds number (Re_{pipe}) of 19 280, based on pipe bulk velocity and pipe diameter. This value of Re_{pipe} is high enough to warrant the use of a standard $1/7$ power law profile to model the velocity profile in the pipe. With such a profile, the ratio between centreline velocity and bulk velocity is approximately 1.22. Since velocity ratio, R, is based on crossflow velocity and pipe bulk velocity, with $R = 4.0$, $U_{jet} = 4.0U_\infty$. Then, using the value given by the $1/7$ power law, we find that the centreline velocity, $V_c = 4.9U_\infty$. In the measurements reported by SP, the jet centreline velocity as it emerges from beneath the flat plate is only $4.3U_\infty$. This discrepancy probably occurs because the pipe flow used in the experiments of SP was not fully developed by the time it emerged into the main test section. S. A. Sherif (personal communication) confirms that the length of the inflow pipe was not sufficient to guarantee a fully developed profile. Setting the velocity ratio at 3.3 is an attempt to match the centreline velocity of our temporal pipe with the centreline velocity given by SP. In figure 4 notice that at $z = 0$ the centreline velocity of Case 3I matches that of SP. When we increase Re_D for Case 3II, the resulting centreline velocity is too low, but we choose to hold R constant in order to better isolate the effects of Re_D. Increasing Re_D to the same magnitude as that used by SP would have required significantly more grid points to achieve sufficient flow resolution. Because computational resources are limited, we only doubled Re_D, and this proved sufficient to demonstrate clearly the effects of Re_D.

4.2. *Flat-plate boundary layer differences*

SP used flow tuft visualizations to establish that their flat-plate boundary layer was laminar when the jet flow was turned off. However, an analysis of the flow conditions of SP shows that their laminar boundary layer was very close to transition. They list the characteristics of their laminar flat-plate boundary layer over the jet exit (with no jet flow) as

$$\delta_{99} = 6.9 \text{ mm}; \quad U_\infty = 0.35 \text{ m s}^{-1}, \tag{4.2}$$

where δ_{99} is the 99% boundary layer thickness. From these values we can estimate the momentum thickness of the boundary layer, θ, using well known correlations for a Blasius boundary layer. Using this estimate of the momentum thickness, we compute a Reynolds number based on the momentum thickness, $Re_\theta = 320$. Kays & Crawford (1980) list the value of the critical Re_θ for transition from a laminar to a turbulent boundary layer as 162, for a variety of flow conditions. Although SP specified that their boundary layer was laminar, its Re_θ indicates that it was very close to transitioning. Upon encountering the perturbation introduced by the jet, the boundary layer probably transitions rapidly to a fully turbulent one. The Re_θ of the simulations are 70 and 140 for Cases 3I and 3II, respectively. Thus, the flat-plate boundary layers in the simulations are well below the critical Re_θ and do not transition as readily to turbulence. The higher velocities we observe in the lower portions of the

computed profiles are due to differences between the flat-plate boundary layers in the simulations and the experiments.

The flow field in the wake behind the jet has been shown to be highly complex (Fric & Roshko 1994; Kelso *et al.* 1996), containing both upright and streamwise oriented vortices. Since vorticity for these structures originates only from the flat-plate boundary layer, its nature is of critical importance. A turbulent boundary layer would provide a stronger source of vorticity which might result in stronger, more frequent structures. Thus, the flow measured by SP over a turbulent boundary layer would have lower mean velocities and higher levels of turbulent fluctuation than a similar flow over a laminar boundary layer, as we observe.

Given the uncertainties in the experimental configuration of SP, the overall agreement between simulations and experiment is quite good, reinforcing our assessment that the numerical simulations produce an accurate representation of the flow physics.

5. Coherent vortical structures

Fric & Roshko (1994) and others have categorized the coherent structures into four groups: jet shear layer vortices, horseshoe vortices, wake vortices, and the counter-rotating vortex pair (CVP). We observe all of these structures in our simulations and find that the majority arise from vortical interactions within the jet shear layer in the near field of the jet. Thus, to better understand the formation of the structures described by Fric & Rosho (1994), we must first look at near-field structures. We then look at how the CVP arises from near-field interactions and examine the weaker structures found in the jet wake.

5.1. *Near-field structures*

To illustrate the variety of different vortical structures formed from the jet shear layer in the near field, we examine two flow quantities, vorticity and pressure; they are plotted as isosurfaces in figure 5(*a,b*). Regions of high vorticity often mark the locations of coherent structures, but can also mark regions where no structures are present. Also, the spatial variability of the vorticity magnitude is quite high, and this can obscure large-scale features. Pressure isosurfaces mark the locations of the low-pressure cores of vortical structures and provide another means of visualizing large-scale features in the flow field. Together, the two quantities provide a more complete picture of the flow field. In figure 5(*a*), we combine three different isosurfaces within a single plot. The green isosurface marks regions in the flow where $|\omega_x| = 20.0$, the blue surface marks the same magnitude for $|\omega_y|$, and the red surface marks the same magnitude for $|\omega_z|$. Of course, regions exist where more than one component of vorticity is significant, but in such regions, the component which covers the greatest volume in the flow field obscures the isosurfaces of the remaining components. Visualizing the flow in this manner allows one to see how vorticity aligned in a particular coordinate direction can tilt into other directions. From figure 5(*a*) we immediately see that the JICF is not composed of an orderly progression of vortex rings, but instead contains an extensive array of different vortical structures. For ease of discussion, we have given the following names to the structures: hanging vortices, spanwise rollers, and vertical streaks, as indicated in the figure. In figure 5(*b*), we plot pressure relative to the free-stream pressure, defined as $\tilde{p} = (p - p_\infty)/\rho U_\infty^2$.

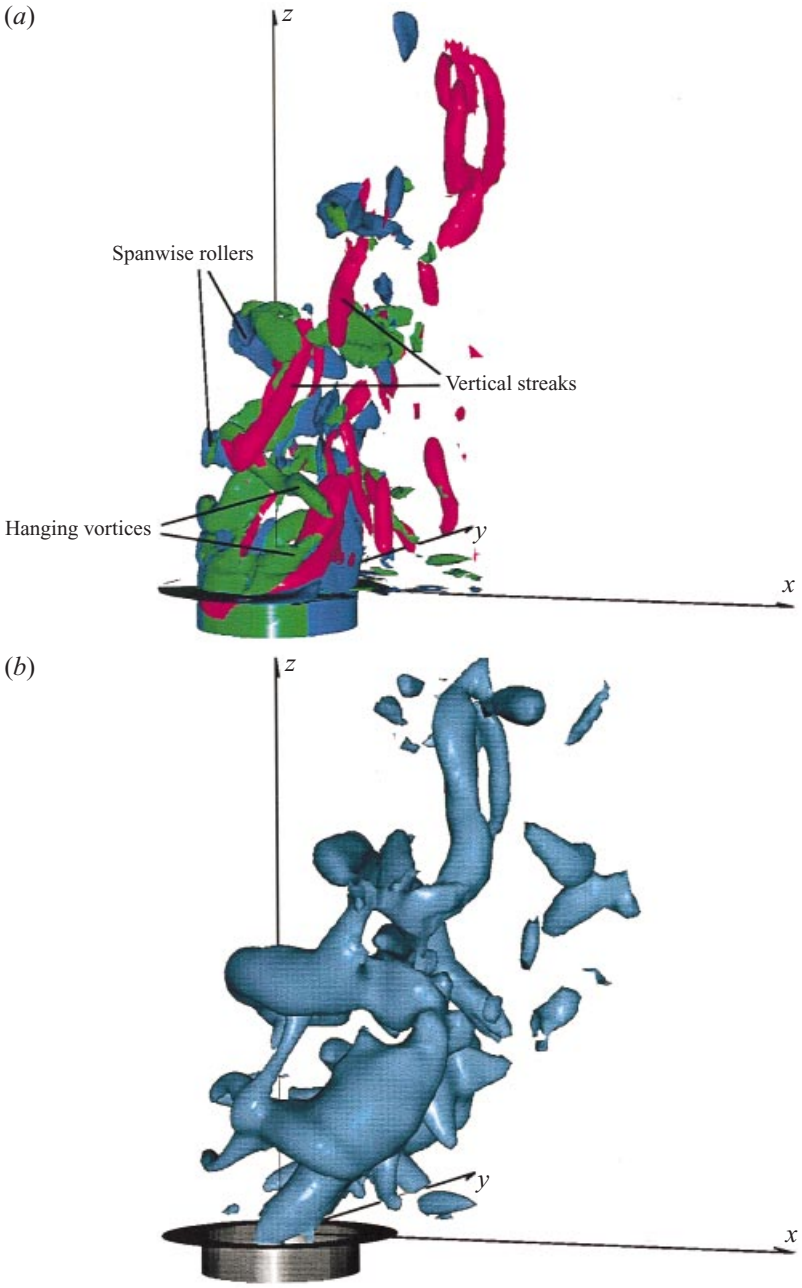

FIGURE 5. (*a*) Isosurfaces of vorticity. Green: ω_x, blue: ω_y, red: ω_z. $|\omega| = 20.0$. (*b*) Isosurfaces of pressure. $\tilde{p} = -1.8$.

5.1.1. *Hanging vortices*

Kelso *et al.* (1996) marked the jet shear layer by injecting dye into their jet through a circumferential slot located 1.6D below the flat plate. They observed that a large fraction of the dye collected in tube-like structures which began directly above the exit on the lateral edges of the jet. These tubes, one on each side of the jet, extended

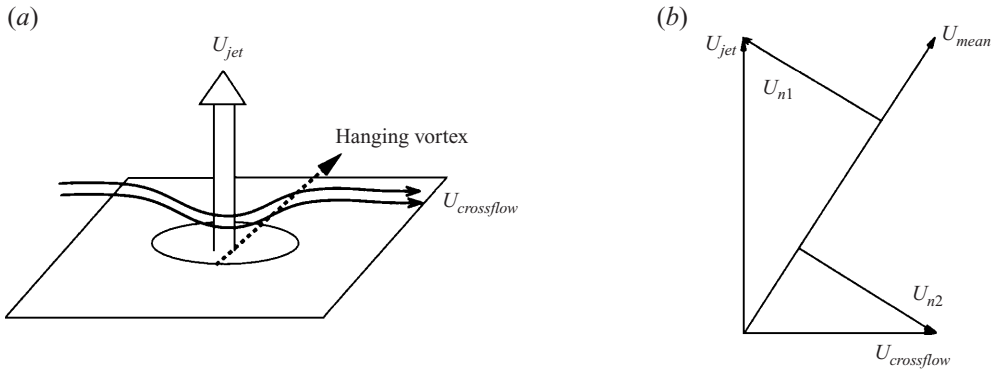

FIGURE 6. (*a*) Hanging vortex and orientations of jet and crossflow velocities. U_{jet} is the bulk velocity of the incoming jet, and $U_{crossflow}$ is the mean streamwise component of the crossflow velocity. (*b*) Vector sum of relevant velocities.

around the jet body and then up along the back side of the jet, roughly matching the jet trajectory. Kelso *et al.* (1996) hypothesized that the tubes marked the location where the jet shear layer folded and rolled up into a vortex. They also proposed that vorticity found in these tubes contributed to the circulation of the CVP. We observe the same phenomenon in our simulations. Directly above the jet exit in figure 5(*a*), two vortical structures are clearly evident. One begins directly at the exit on the lateral edge of the jet and extends up and around the jet body, while the second is located approximately $0.3D$ above the first and extends horizontally along the lateral edge of the jet. We have named these vortical structures the hanging vortices.

The hanging vortices do not shed regularly into the main flow. Instead, the lower hanging vortex is a quasi-steady structure which oscillates around a fixed location. The upper hanging vortex behaves in an unpredictable manner. At times, it will shed into the main flow, and a new vortex will form to replace it. At other times it will fold upon itself and shed vertical vorticity from this internal interaction. Haven (1996) observes similar structures in her experimental flow visualizations. In a transverse slice downstream of the jet, she finds a pair of 'unsteady' counter-rotating vortices that ride on top of a 'steady' pair of vortices.

The hanging vortices arise from the Kelvin–Helmholtz (K–H) instability between the jet and the crossflow. As the crossflow deflects around the jet body, it accelerates on the lateral edges, reaching velocities as high as $1.8U_\infty$. Thus, on the lateral edges of the jet, a mixing layer forms between two streams of fluid whose velocities are not parallel (figure 6). Mixing layers formed from non-parallel streams are referred to as skewed mixing layers. They have been studied in great detail, most recently by Lu (1995). He found that the vortical structures formed in these layers grow in the direction of the mean convective velocity and that they carry a strong axial flow. To clarify this point, in figure 6 we have also drawn the orientations of the relevant velocities. To estimate the orientation of the K–H instability, we decompose each velocity into components parallel to the mean velocity (U_{mean}) and normal to the mean velocity (U_{n1} and U_{n2}). The vortical roll-up should be approximately normal to $U_{n1} - U_{n2}$ and approximately parallel to U_{mean}. In Case 3II, the mean magnitudes of U_{jet} and $U_{crossflow}$ at this location are approximately $3.3U_\infty$ and $1.8U_\infty$, respectively. The hanging vortex we observe extends upwards and downstream from the jet exit, as would be expected based on the preceding analysis. We also observe a strong axial flow through the hanging vortex, a result of the mean velocity of the two streams.

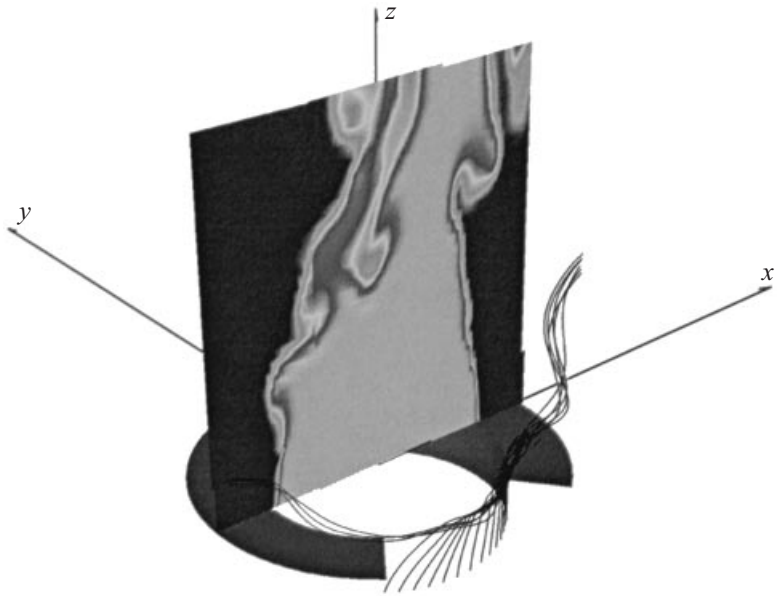

FIGURE 7. Instantaneous streamlines through a hanging vortex. Partial scalar contours on the centreplane also shown for perspective.

The hanging vortices produce several interesting effects which have important consequences for the downstream behaviour of the jet. The strong axial flow in each vortex transports a significant amount of scalar concentration, vorticity, and vertical momentum away from the jet body. In essence, the hanging vortex provides a path downstream for jet fluid. In figure 7 we have plotted two sets of instantaneous streamlines. One set originates within the jet, $0.03D$ from the pipe wall and $0.25D$ below the surface of the flat plate. Notice how streamlines from a wide expanse of the lateral edge of the jet all collect in the hanging vortex. The second set originates from the crossflow boundary layer upstream of the jet exit. These lines also collect in the hanging vortex. Based on these streamlines, it appears that the fluid transported downstream by the hanging vortex originates primarily from the near-wall region of the pipe flow and from the crossflow boundary layer.

Because the mixing layers on the sides of the jet are skewed, we believe that it may be misleading to view the vortical roll-ups in the JICF as vortex rings. Vortex rings have been used quite often to interpret the flow physics and as a basis for developing theories for the formation of the CVP (Kelso *et al.* 1996; Andreopoulos 1985; Sykes *et al.* 1986). However, as we have described, the vortices on the sides of the jet differ fundamentally from those that appear in vortex rings because they do not shed regularly downstream and because they carry a strong axial flow through their cores. One consequence that develops from this new view of the near-field vorticity dynamics is a new CVP formation mechanism, which we describe in the rest of this section.

Based on their flow visualizations, Kelso *et al.* (1996) hypothesized that a vortex breakdown occurs in the hanging vortex, and we observe this phenomenon in our flow. The breakdown process is probably instigated by two mechanisms. First, on the lateral edge of the jet, velocities are high and pressures low; so, as the vortex moves downstream from the lateral edge of the jet, it encounters an adverse pressure

FIGURE 8. Vortex lines through the hanging vortex. Isosurface of pressure at $\tilde{p} = -3.6$ included to show locations of structures.

gradient. Secondly, we observe a strong upstream flow in the wake of the jet (see §6.1), which generates compressive stresses on the lee side of the jet. The combination of these two factors leads to vortex breakdown.

We can best observe this breakdown process by examining vortex lines drawn through the hanging vortex (figure 8). Vortex lines are created from the simulation data simply by computing lines which are everywhere tangent to the vorticity vector field. In the figure, an isosurface of pressure is included to help identify the location of the hanging vortex. The vortex lines entering the bottom of the vortex are relatively parallel, and they continue to be aligned up to the end of the region marked by the isosurface. At this point, a slight bulge in the pressure isosurface marks the start of the breakdown, and the vortex lines begin to spread. Eventually, little sign of the original vortex remains in the tangle of vortex lines. The rapid spreading of an initially compact group of vortex lines is clearly indicative of a vortex breakdown.

Vortex breakdown is also characterized by a sudden decrease of the axial velocity through the vortex. To examine the evolution of the velocity through the hanging vortex, we selected one of the streamlines from figure 7 and computed the velocity along it. In figure 9, we plot projections of the streamline onto the (x, y)- and (x, z)-planes and compare to a plot of the velocity along the streamline. The evolution of the hanging vortex becomes clear as we examine the development of the axial velocity. We first see an initial region in which the vortex develops and axial velocity increases. Then, the magnitude of the velocity decreases gradually, indicating a slow expansion of the vortex core. At $x \approx 1.2$ we observe a sudden drop in velocity which marks the vortex breakdown. This decrease is accompanied by marked changes in the path of the streamline. In figure 7 also notice that the streamlines turn sharply toward the centreplane at $x \approx 1.2$. After the breakdown, the vortex loses coherence,

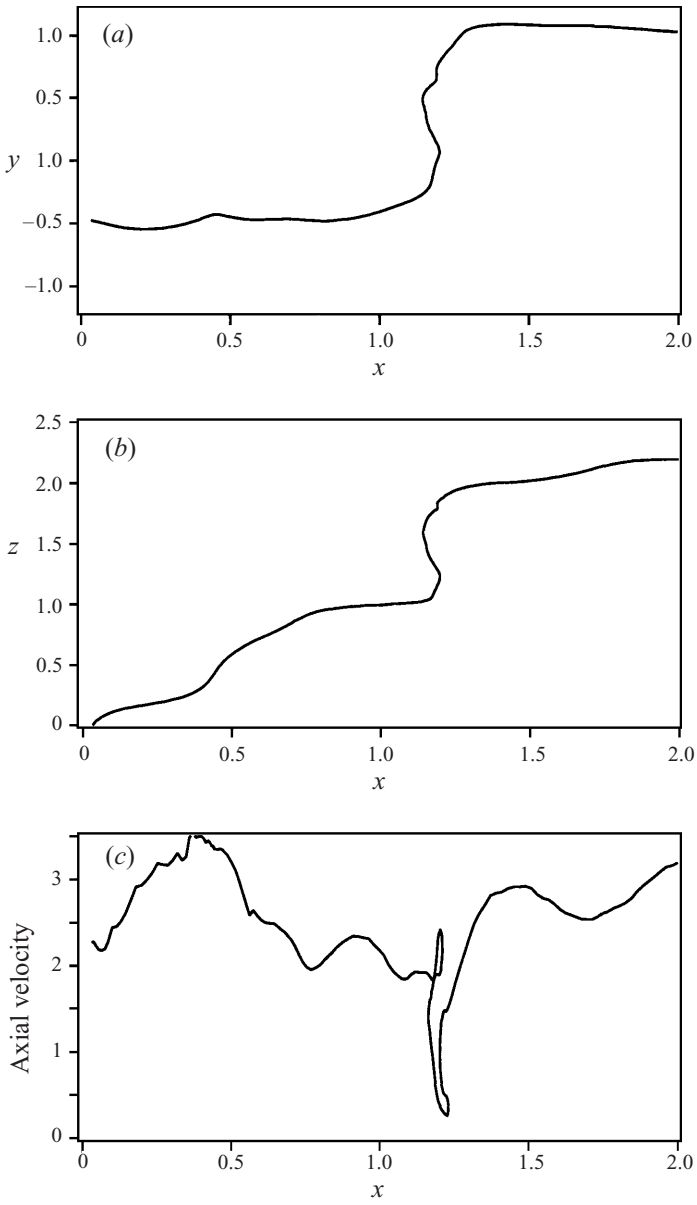

FIGURE 9. Evolution of axial velocity through the hanging vortex. (*a*) Projection of streamline onto the (x, y)-plane. (*b*) Projection of streamline onto the (x, z)-plane. (*c*) Instantaneous axial velocity along streamline. (NB: Here, and in all subsequent plots, all distances are non-dimensionalized by the jet diameter, D; plotted quantities are non-dimensional as well (see §2).

and the streamlines no longer indicate the path of the hanging vortex. Instead, the streamlines follow the local small-scale turbulence field, which in this case, moves fluid toward the centreplane.

The fluid found in a hanging vortex on one side of the jet originates only from the shear layer on the same side of the jet, so the direction of the fluid rotation is of a single sign, $\omega_x > 0$ and $\omega_z > 0$ on the left-hand side of the jet and $\omega_x < 0$ and $\omega_z < 0$ on the right (looking upstream). We can best see the left–right dependence of the sign

FIGURE 10. Isosurfaces of vertical vorticity, back view. Light grey surface value: +20, dark grey surface value: −20. Direction of crossflow is out of the page.

of the vorticity by examining the isosurfaces of vertical vorticity plotted in figure 10. At the bottom of the jet, notice that the left-hand side is dominated exclusively by $\omega_z > 0$ and the right-hand side dominated by $\omega_z < 0$. Contrast this distribution of vorticity with locations higher in the jet trajectory, where a clear distinction does not exist, and positive and negative vorticity can be found on both sides of the jet. After the vortex breakdown, the left–right dependence of the sign of vorticity is retained, and a weak CVP is formed. Once the breakdown occurs, the velocities within the hanging vortex are low enough that they can be turned by a small pressure gradient and aligned with the trajectory of the jet.

Hence, the CVP apparently originates from quasi-steady vortices that form in the skewed mixing layers on each lateral edge of the jet. These vortices encounter adverse pressure gradients on the lee side of the jet and break down into a pair of weak counter-rotating vortices that are aligned with the jet trajectory.

5.1.2. *Spanwise rollers*

Near the centreplane on the upstream and downstream edges of the jet, spanwise and streamwise velocities in the crossflow are relatively small, and the K–H instability produces the well-known roller structures. The nature of the K–H instability changes as we move azimuthally around the jet and horizontal velocities increase (as noted in §5.1.1). Thus, we do not observe the formation of vortex rings around the periphery

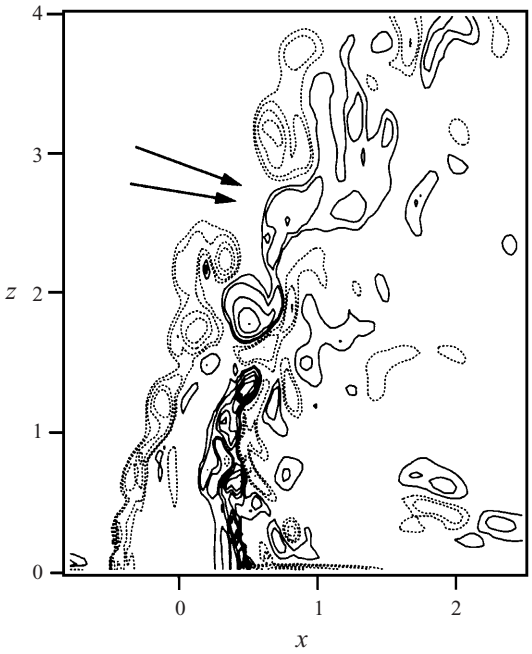

FIGURE 11. Instantaneous contours of ω_y showing jet shear layer vortices. Contour interval: $\omega_y \approx 10.0$. Location of intrusion of crossflow fluid indicated by arrows. Dotted contours indicate negative values.

of the jet. Instead, we only find regular formation of spanwise rollers on the upstream and downstream edges.

These rollers are best seen in instantaneous contours of spanwise vorticity (ω_y) near the jet on the centreplane (figure 11). Vortices form in the upstream shear layer earlier and more regularly than in the downstream layer, where the vortex roll-up is irregular and can be delayed until $z \approx 1.5$. This difference may be caused by the different pressure gradients found on the upstream and downstream edges of the jet. On the upstream edge, an adverse vertical pressure gradient forms as a result of the velocity gradient in the crossflow boundary layer: the lower streamwise velocities near the wall produce a lower stagnation pressure than velocities in the free stream. As a result of this adverse pressure gradient, the upstream shear layer becomes unstable soon after emerging into the flow and rolls up into vortices. The downstream shear layer issues into the low-pressure lee side of the jet and sees a favourable pressure gradient, which enhances its stability and delays vortex roll-up.

At $z \approx 2.0$, the rollers formed from the upstream and downstream shear layers, which have opposite signs, interact in an unpredictable manner, creating gaps in the jet flow on the order of one jet diameter. One such gap can be seen in figure 11 centred around $x \approx 0.5$ and $z \approx 2.7$. The gaps produced by these vortex interactions on the upstream edge of the jet prove to be an important mechanism for entrainment of crossflow fluid by the jet.

The spanwise rollers are strong, energetic structures which penetrate deeply into the crossflow, defining the upper boundary of the jet. Jet fluid carried by the hanging vortex rapidly acquires horizontal momentum and follows a lower trajectory. This fluid initially fills the lower portions of the jet cross-section and defines the bottom of the jet body. At stations close to the jet exit, the spanwise rollers occasionally

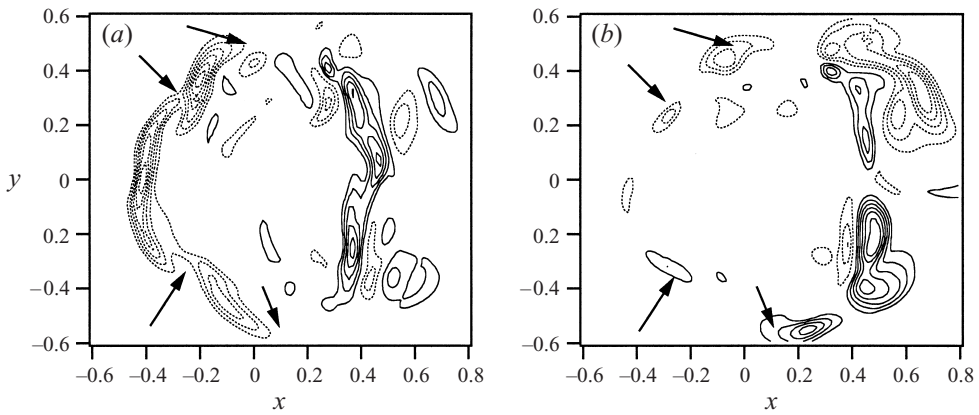

FIGURE 12. Plan view of vorticity contours. (*a*) ω_y, (*b*) ω_z. Dotted contours indicate negative values. $z = 0.35$.

rise fast enough to create a gap of nearly irrotational fluid in the middle of the jet cross-section.

The stability of the initial jet shear layers may explain the strong Re_D dependence we observed in the vertical profiles of §4. The onset of instability and the subsequent vortical roll-up occurs later in the trajectory of the lower-Re_D jet. The rollers produced by the lower-Re_D jet then penetrate more deeply into the crossflow. Thus, the vertical location of the velocity maximum is higher at low Re_D. Downstream, the spanwise vorticity found in the rollers is tilted into other directions and dispersed; so, by $x \approx 4$, these structures have largely disappeared.

5.1.3. *Vertical streaks*

In addition to the spanwise rollers, the other feature we find in the main jet body is streaks of vertical vorticity. These streaks form when irregularities, or kinks, within each spanwise roller are stretched vertically by the local strain field, in a manner similar to the formation of ribs observed in plane mixing layers (Moser & Rogers 1993). We observe this phenomenon in a plan view of spanwise and vertical vorticity contours through a single roller (figure 12*a*, *b*). The majority of the production of vertical streaks occurs in the upstream rollers. In figure 12(*a*), contours of ω_y appear in several distinct structures, and in the gaps between these structures (marked by arrows) we find ω_z structures (figure 12*b*). On the negative-y half of the plane, $-\omega_y$ is tilted into $+\omega_z$, while on the positive-y half of the plane $+\omega_y$ is tilted into $+\omega_z$. These patterns are consistent with a mechanism in which a small perturbation deflects the upstream roller into the interior of the jet. So, in the vicinity of the perturbation a small amount of spanwise-oriented vorticity (ω_y) is changed to streamwise vorticity (ω_x). This streamwise vorticity is then tilted by gradients in the mean vertical velocity ($\partial W/\partial x$) to form a streak of vertical vorticity (ω_z). Because the horizontal gradients of vertical velocity are very high, any slight perturbation in the spanwise rollers can produce a vertical streak.

These vertical streaks appear consistently in the near field of the jet and persist until the jet bends into the crossflow direction. In the bending region, the vertical structures are tilted into the streamwise direction by the mean strain field created by the curved flow field, and dispersed further by the local turbulence field. Eventually, they simply contribute to the turbulent mix of vorticity in the far field.

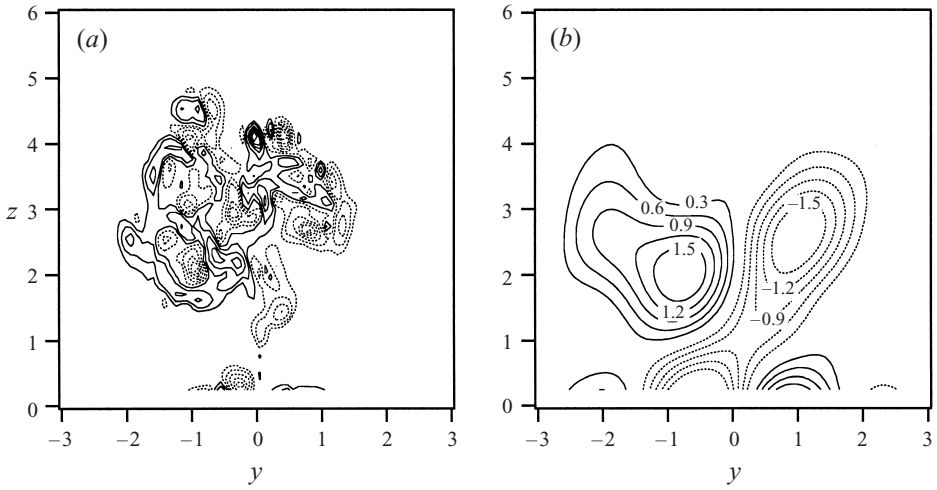

FIGURE 13. (*a*) Instantaneous streamwise vorticity; (*b*) has been low-pass filtered. $x = 2.5$.

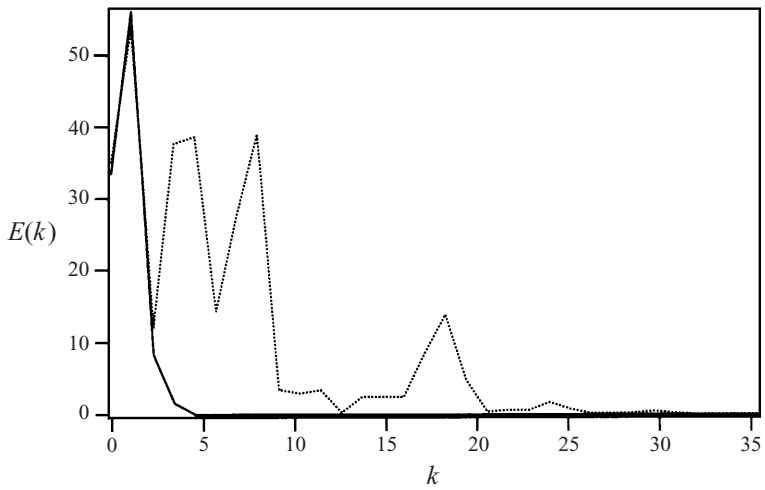

FIGURE 14. One-dimensional power spectra of ω_x on a spanwise line located at $x = 2.5$ and $z = 3.0$. Dotted line: unfiltered vorticity. Solid line: filtered vorticity.

5.2. *Counter-rotating vortex pair*

We have presented a mechanism by which the vorticity carried by the hanging vortex provides the circulation necessary to create the CVP. However, the hanging vortex only accounts for a fraction of the total circulation flux carried by the jet. The remaining jet vorticity can be found in the spanwise rollers and vertical streaks which follow a higher trajectory in the flow field. As these structures bend in the crossflow, they break down into a very intense turbulent field, and the weak circulation provided by the CVP is a background rotation for this turbulent field. If this interpretation is accurate, one should be able to extract the background circulation from instantaneous realizations of the flow field.

We extract the instantaneous signature of the CVP by low-pass filtering the instantaneous streamwise vorticity on transverse planes. The filter used is a standard low-pass Butterworth filter (Krauss, Shure & Little 1994) with a cutoff wavenumber

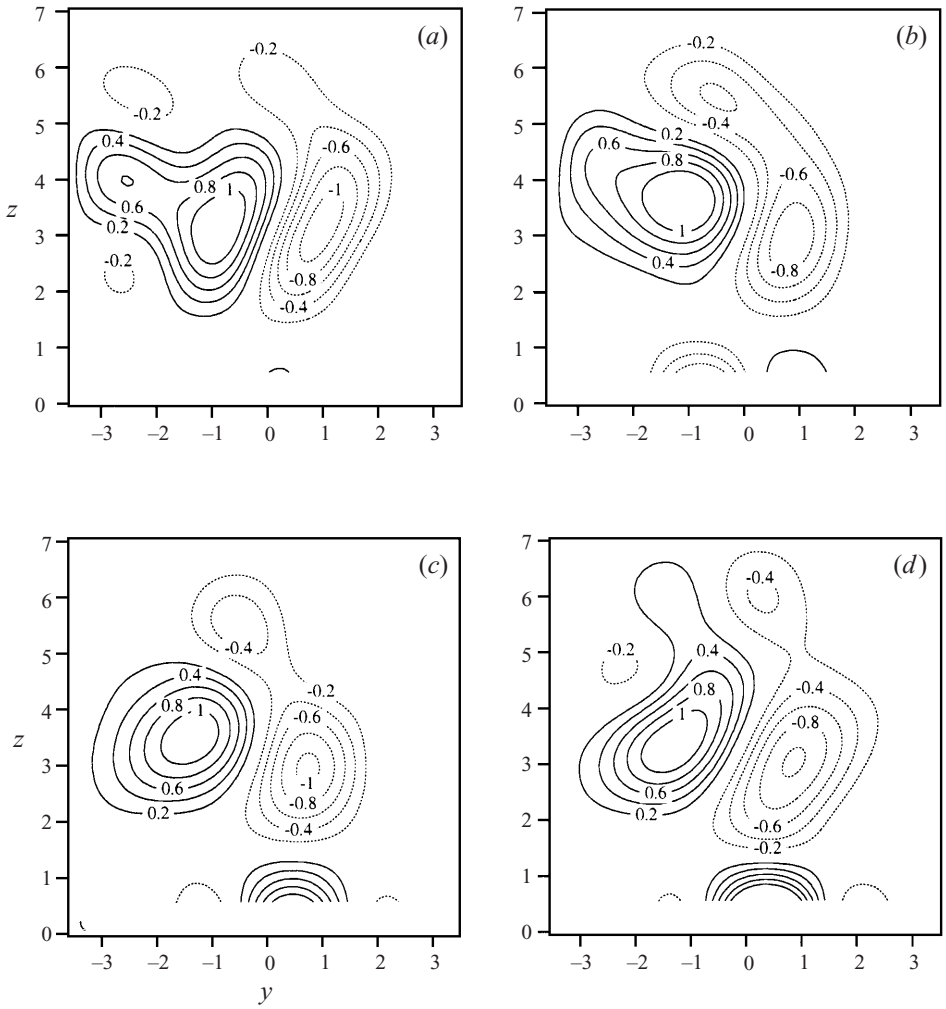

FIGURE 15. Spatial evolution of low-pass filtered ω_x. (*a*) $x = 4.5$, (*b*) $x = 5.0$, (*c*) $x = 5.5$, and (*d*) $x = 6.0$. Contour intervals as marked. Dotted contours indicate negative values.

determined by the local width of the jet. To demonstrate the effect of this filter, we present streamwise vorticity on a transverse plane at a single instant in time (figure 13). In (*a*) we plot the full streamwise vorticity field and in (*b*) the filtered streamwise vorticity field. The CVP is evident in the filtered vorticity field and has a maximum vorticity magnitude approximately an order of magnitude lower than those found in the unfiltered vorticity. Notice that at this location, near the jet exit, the CVP is located in the lower half of the jet cross-section.

One can see the effects of the filter more clearly by examining the spanwise one-dimensional power spectrum of the streamwise vorticity plotted in figure 14. It was computed at the same instant and streamwise location as figure 13 on the line $z = 3.0$. The unfiltered spectrum shows several distinct peaks up to $k \approx 30$. In the filtered spectrum, all of these peaks except the first have been suppressed. This first peak is the signature of the CVP. Spectra recorded at other locations and times show similar characteristics.

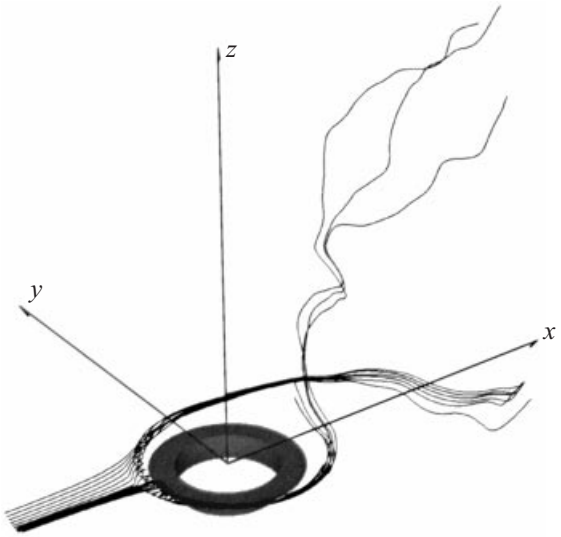

FIGURE 16. Instantaneous streamlines showing the horseshoe vortex.

Several features of this instantaneous CVP should be noted. Firstly, the CVP observed in the filtered vorticity field changes position and strength with time and streamwise location. In figure 15, we plot low-pass filtered ω_x contours at four transverse locations, each separated by $0.5D$, at a single instant in time. The slight changes in position are apparently due to the behaviour of the hanging vortices from which the CVP originates. Small fluctuations in the relative strength of the two vortices would produce the transverse motions we observe.

Secondly, the magnitude of the vorticity in the CVP decays at a much slower rate than the fluctuating vorticity in the rest of the flow field. Figure 15 shows that the sizes and strengths of the vortical regions barely decrease over the streamwise distance covered. Over this same length, maximum vorticity observed in the unfiltered velocity field decays by approximately 20%. This behaviour is expected, as turbulent motions at higher wavenumbers are damped more quickly by viscous dissipation. Farther downstream, as small-scale motions decay further, the CVP becomes the dominant motion observed.

Finally, for lower-Re_D flows, one would expect that a larger fraction of jet fluid would be rolled into the hanging vortices and advected downstream in the CVP. At extremely low Re_D, all the jet fluid may be carried by the hanging vortices on either side of the jet, and the spanwise rollers would not form. In such cases, the body of the jet downstream is clearly divided into the two distinct vortices of the CVP. Huq & Dhanak (1996) observed this phenomenon in their experiments with very low Re_D (<210) jets.

5.3. *Wake vortices*

We observe two vortical structures in the wake of the jet: streamwise vortices which lie close to the wall and vertically oriented (upright) vortices extending down from the jet body to the wall. These structures are closely connected to the horseshoe vortex which forms upstream of the jet. The horseshoe vortex, which is similar to those found upstream of bluff bodies, forms as the crossflow deflects laterally around the jet and stretches spanwise vorticity present in the flat-plate boundary layer. The instantaneous

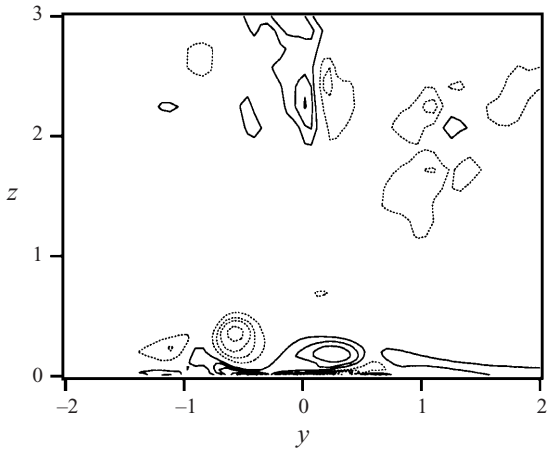

FIGURE 17. Instantaneous contours of ω_x showing wake wall vortices. Transverse slice at $x = 3.6$. Dotted contours indicate negative values.

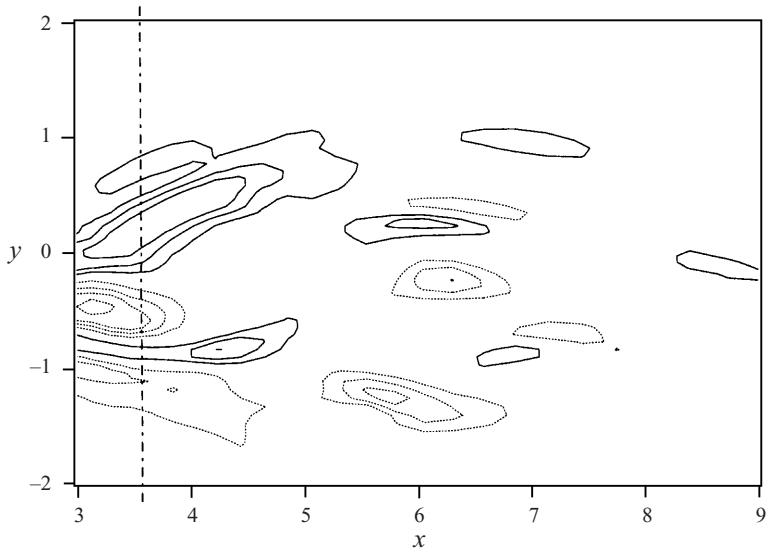

FIGURE 18. Instantaneous contours of ω_x showing wake wall vortices. Plan view at $z = 0.2$. Dotted contours indicate negative values. Dashed line indicates approximate location of the transverse slice in figure 17.

streamlines plotted in figure 16 clearly show this vortex forming upstream of the jet. The legs of the vortex extend around the jet, and on one side, the leg is entrained into the jet and reoriented into the vertical direction while on the other side, the leg simply extends downstream in the wake. Thus, the vortical structures found in the wake of the jet appear to originate from the legs of the horseshoe vortex.

To visualize the streamwise vortices near the wall, we plot contours of streamwise vorticity on a transverse plane in figure 17. The vortical structures of the main jet body are evident at the top of the plot, but we focus our attention on the near-wall region. The vortex on the left is negative in sign, indicating clockwise rotation (looking upstream). This direction of rotation is what we would expect for the leg

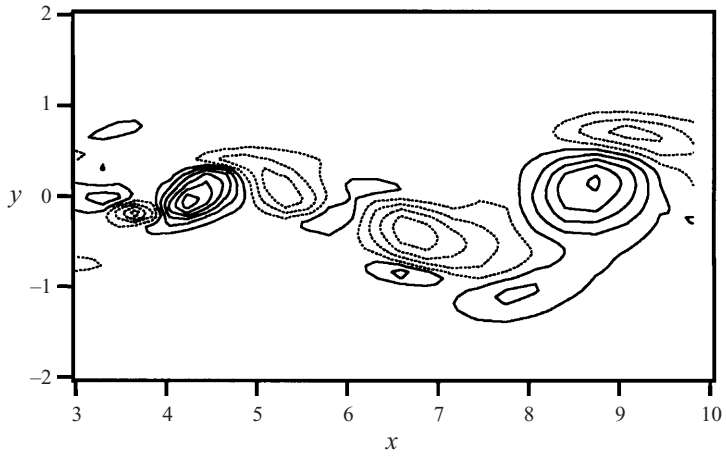

FIGURE 19. Plan view of contours of ω_z at $z = 1.9$ showing wake vortices. Contour interval $\omega_z \approx 0.4$. Dotted contours indicate negative values.

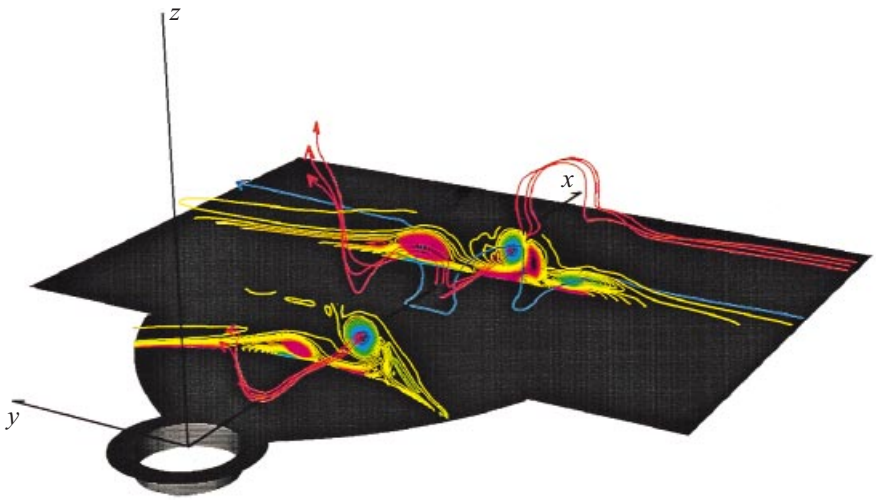

FIGURE 20. Perspective view of vortex lines in the wake. Contours of ω_x on two transverse planes also shown.

of the horseshoe vortex which wraps around the left side of the jet. The vortex on the right is positive, as would be expected also. The wall wake vortices are usually unequal in strength and vary greatly in transverse location.

To better understand the streamwise development of the wall vortex, we look at a plan view at $z = 0.2$ for the same instant in time (figure 18). The vortices are elongated in the streamwise direction, typically ranging in length from $1D$ to $2D$. The strong left-side vortex we observed in the transverse slice is actually quite short in streamwise extent, extending only $1D$ downstream. The vortices become more sporadic with increasing downstream location, and the transverse area in which they appear widens. For the most part, negatively signed vortices appear only on the negative-y half of the domain, and positively signed vortices appear on the other

half. The small regions of vorticity of the 'wrong' sign are secondary vortex structures which are induced by the action of the primary vortex.

Vertically oriented vortices connecting the jet body to the wall have been observed in numerous experiments, most recently by Fric & Roshko (1994) and Kelso *et al.* (1996). From the simulation data, we can best visualize these structures by looking at a plan view of vertical vorticity (ω_z) downstream of the jet, as shown in figure 19. Here, we see a progression of structures, reminiscent of a Kármán vortex street behind solid cylinder. However, the wake vortices do not strictly alternate in sign; two vortices with negative rotations are adjacent to each other in the centre of the plot. Also, as pointed out by Fric & Roshko (1994), the vorticity found in a Kármán vortex street originates from the solid boundary of the cylinder. In the jet in crossflow, no comparable solid boundary exists, so the generation mechanism must be different.

The upright vortices arise directly from an interaction between the horseshoe vortices and the vertical jet flow. We observed this phenomenon in figure 16 where an upright vortex forms as a leg of the horseshoe vortex is entrained and lifted by the jet. However, streamlines do not necessarily show the true behaviour of vortical structures. We can more clearly understand the physics of the flow by looking at instantaneous vortex lines through the vortices located near the wall (figure 20). Contours of streamwise vorticity on two transverse planes are also shown to aid in visualizing the streamwise vortices at the wall.

We first discuss the downstream set of vortex lines drawn in red. They begin on the edge of the domain, oriented in the spanwise direction, as would be expected for vorticity associated with the flat-wall boundary layer. As they approach the centre of the domain, they turn upstream and pass through the core of the near-wall vortex. The vortex lines follow the vortex core upstream for a distance of approximately $1.5D$ and through a sharp turn into the vertical direction. These vortex lines provide compelling evidence that the upright vortices are vertical extensions of wall structures, and the vorticity in the upright vortices originates from the flat-wall boundary layer (in agreement with the findings of Fric & Roshko 1994). The reorientation of wall vortices seems to occur directly behind the jet. We hypothesize that the upstream end of a wall vortex is entrained into the underside of the jet by the roll-up that produces the hanging vortices. In figure 20 we see the latter stages of this process in the set of vortex lines near the jet exit.

In the current set of simulations, wall vortex reorientation occurs in an unpredictable manner, producing vortices without a discernible pattern. Some vortices remain close to the wall and do not produce vertical extensions. The blue vortex line in figure 20 marks one such vortex, as it remains close to the wall throughout its path.

In these simulations we find that vorticity in the wake structures (that is, the streamwise vortices near the wall and the upright vortices extending from the wall to the jet body) originates entirely from the flat-wall boundary layer. This finding agrees with the observations of Smith & Mungal (1998). They report that no jet fluid is found in the wake structures for $R < 10$. In cases in which $R > 10$, they do observe that as the streamwise wall vortices are stretched by the vertical jet, they develop a strong enough axial flow to transport jet fluid into the wake. However, at lower velocity ratios, the jet bends over into the cross-stream too rapidly for this process to occur. Not surprisingly then, at the values of R used in our simulations, we find no jet fluid in the wake structures. Thus, it does not appear that jet vorticity is entrained into the wake structures for the flow parameters considered in this study.

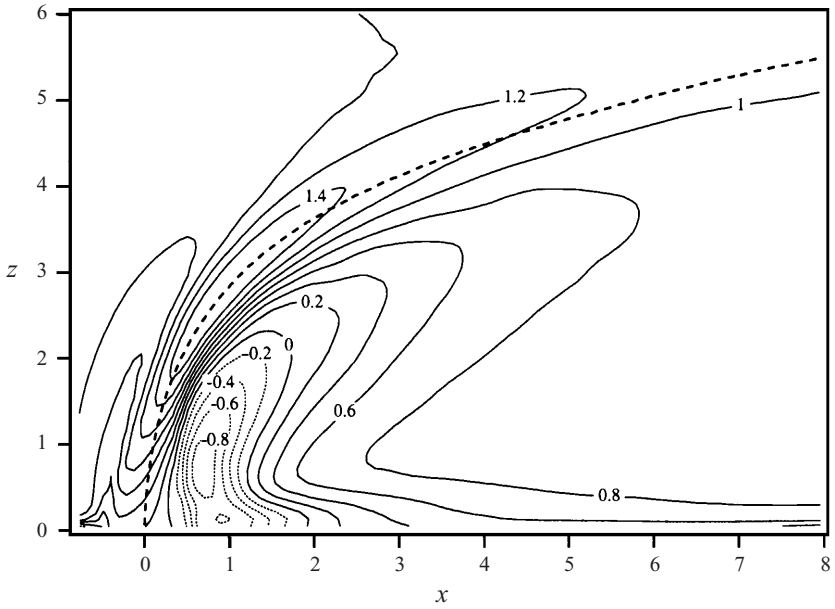

FIGURE 21. Mean streamwise velocity (U) contours at the centreplane. Case 3II. Contour intervals as marked. Heavy dashed line indicates location of mean streamline beginning from the origin.

6. Flow statistics

6.1. *Mean flow*

In the interest of conciseness we present only statistics from Case 3II, as the other cases are qualitatively similar. Also, we confine much of our presentation to centreplane statistics although many interesting phenomenon occur off the centreplane. For more complete results, please refer to Yuan (1997). In the following sections, the resolved velocity, u_i, has been decomposed into mean and fluctuating quantities according to the following expressions: $U_i = \langle u_i \rangle$ and $u_i'' = u_i - U_i$, where again $\langle\ \rangle$ represents a long time average. Also, (U, V, W) represent the mean velocities in the streamwise, spanwise, and vertical directions, respectively, and will be used interchangeably with U_i.

In figure 21 the heavy dashed line indicates the location of the mean streamline which begins at the origin. We include this line in all subsequent centreplane contour plots, as it places the mean trajectory of the jet and facilitates comparison between different plots. Near the flat plate, the crossflow slows and stagnates as it approaches the jet exit. Higher up, as the crossflow deflects over the bending jet, it accelerates to a maximum value of approximately 1.5 times its free-stream value. In the region where the jet flow is strongly curved ($x \approx 1.0$), the location of maximum streamwise velocities lies on the mean jet trajectory, indicating that accelerated crossflow fluid is entrained into the front edge of the jet and incorporated into the main jet body. Further downstream, maximum streamwise velocities lie above the trajectory, indicating that this fluid is pushed upward by the flow created by the CVP.

Directly behind the jet exit, crossflow fluid enters the low-pressure wake and generates an upstream flow with a maximum velocity of about 80% of the free-stream velocity. This upstream flow creates the compressive stresses on the back of the jet which slow the axial velocity through the hanging vortices and trigger the

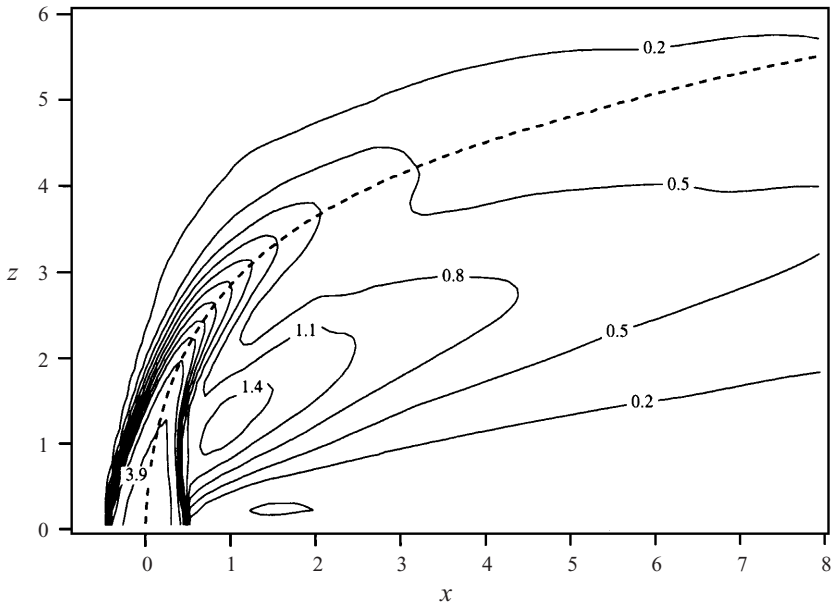

FIGURE 22. Mean vertical velocity (W) contours at the centreplane. Case 3II. Contour intervals as marked.

formation of the CVP. Further downstream near the wall, the contours lines begin to lie parallel to the x-axis, indicating a recovery to a flat-plate boundary layer.

In the contours of mean vertical velocity (figure 22) we see two regions of strong upward motion. The upper region, which begins directly over the jet exit, closely coincides with the mean trajectory, and is due to the vertical momentum of the jet. The magnitude of this vertical momentum decays as jet fluid is dispersed away from the centreplane.

The lower region of vertical velocity forms behind the jet and has a maximum magnitude of about $1.4U_\infty$. This branch of vertical velocity is due to fluid advected downstream through the hanging vortices. After these vortices break down on the back side of the jet, their diameters increase dramatically, and the vortices induce a vertical velocity at the centreplane. The combined effect of the two vortices produces the lower region of vertical velocity.

6.2. *Turbulent kinetic energy*

In figure 23, we plot contours of resolved turbulent kinetic energy (TKE) on the centreplane, $q^2 = u_i'' u_i''/2$, scaled by the square of the initial jet velocity. Because the velocities, u_i'', were non-dimensionalized by the crossflow velocity, this scaling requires dividing q^2 by the square of the velocity ratio (R^2). We present plots for Case 3II only and discuss differences we observe between the different runs. Several features are worth noting. First, the maximum values of $\langle q^2 \rangle$ for all cases (2I, 3I, 3II) are comparable, so scaling with the jet velocity seems appropriate. Secondly, the location of the maximum $\langle q^2 \rangle$ is close to the top of the jet, where the rollers emanating from the downstream and upstream edges collide. This location shifts slightly downstream in the lower-R cases, but remains in the same position relative to the jet exit. Third, the magnitude of $\langle q^2 \rangle$ is quite high along the upstream edges in all cases and decays

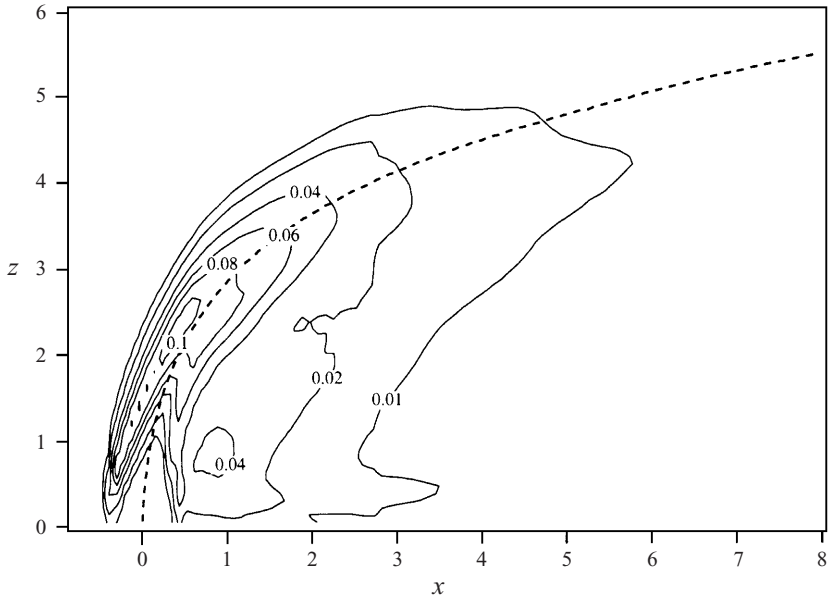

FIGURE 23. Contours of turbulent kinetic energy ($\langle q^2 \rangle / R^2$) at the centreplane. Case 3II. Contour values as marked.

toward the jet interior. All cases also show a local maximum near the wall, due to the velocity fluctuations generated by the wake vortices.

The vertical location of maximum turbulence intensity relative to the mean trajectory shifts with downstream location. Near the jet exit, turbulence is most energetic at the upstream edge of the jet and above the mean trajectory. Downstream, the location of peak turbulence shifts towards the interior of the jet. For example, the downstream edge of the 0.01 contour level lies substantially below the mean trajectory. This shift is due to a change in the main mechanism of turbulence production. At this point, turbulence production by the spanwise rollers is overshadowed by production by the shear between the jet and the crossflow and by the intermittency of the CVP.

We look now at transverse slices of TKE to examine the evolution of turbulence over the entire cross-section as the jet advects downstream (figure 24). On each plot, a single contour of mean streamwise vorticity is drawn to indicate the mean location of the CVP. At the first downstream location ($x = 1.0$), the peak $\langle q^2 \rangle$ values appear in a broad region spanning the middle of the jet cross-section. This region of high $\langle q^2 \rangle$ results directly from the spanwise rollers. Below this local maximum, TKE levels have two distinct lobes, each corresponding to a vortex of the CVP. At this location, maximum TKE intensities are found in the upper half of the cross-section, while the CVP is found in the lower half.

At the next station downstream ($x = 2.4$), the maximum $\langle q^2 \rangle$ region has divided into two discrete lobes. The local minimum at the centre has decreased greatly in size. Although this local minimum diminishes in size, its presence is maintained by the CVP, which advects less turbulent crossflow fluid into the bottom of the jet. At the wall, two local maxima are the results of fluctuations produced by the wall wake vortices. Again, the decay of TKE is very rapid; at this location, only $1.4D$ downstream from the previous slice, maximum TKE levels are less than half their magnitude at the previous station.

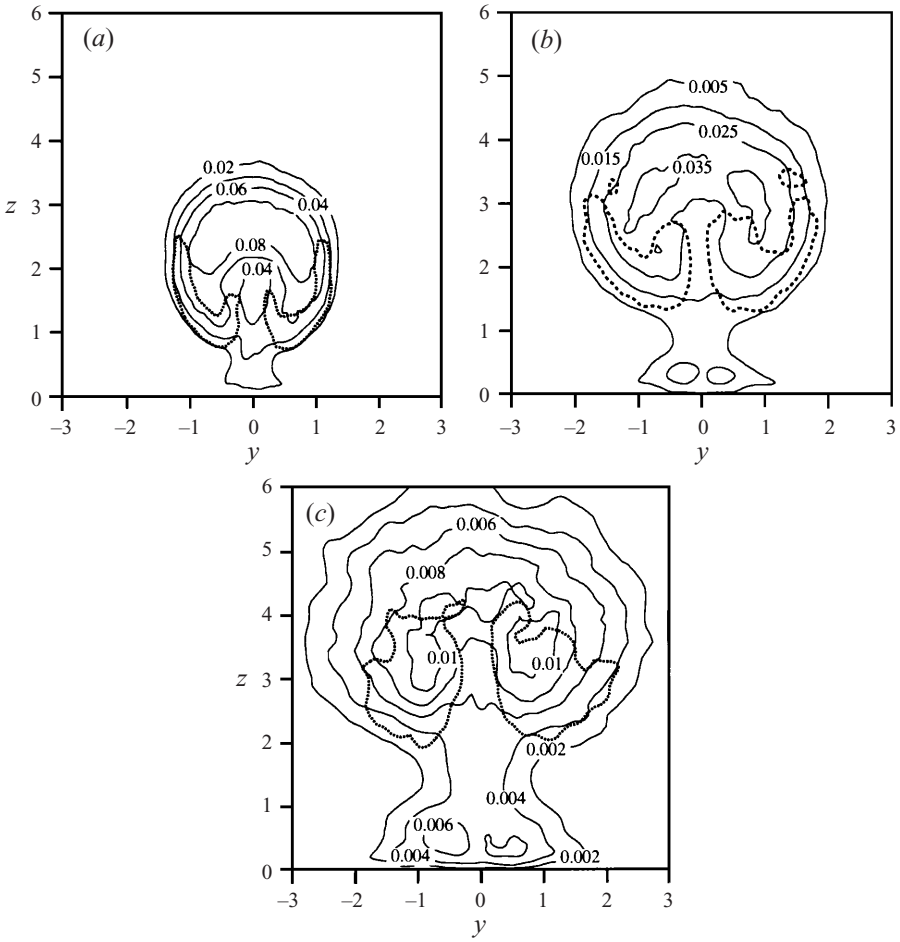

FIGURE 24. Contours of turbulent kinetic energy on transverse planes ($\langle q^2\rangle/R^2$). (*a*) $x = 1.0$, (*b*) $x = 2.4$, (*c*) $x = 5.5$. Case 3II. Contour values as marked. Single contour of $\langle\omega_x\rangle$ drawn as a heavy dotted line on each plot to indicate the location of the CVP.

The decay of turbulence levels at the top (and upstream edge) of the jet appears to be more rapid than in the rest of the jet. This elevated decay is manifested by the downward movement of the points of maximum $\langle q^2\rangle$ within the cross-section. At $x = 1.0$ the maximum $\langle q^2\rangle$ contour is located at the top of the cross-section, and by $x = 5.5$ the local maxima have moved to locations approximately in the middle of the section and into the CVP.

6.3. *Reynolds stress*

In these simulations, the traditional Reynolds stresses (R_{ij}) which appear in the well-known Reynolds-averaged Navier–Stokes equations, consist of resolved and unresolved subgrid-scale contributions as follows:

$$R_{ij} = \langle u_i'' u_j''\rangle + \langle\tau_{ij}\rangle. \tag{6.1}$$

We have monitored the magnitude of the subgrid-scale stresses and have found that at their maximum levels they still contribute less than 5 % to R_{ij}, so we present only the resolved turbulent stresses.

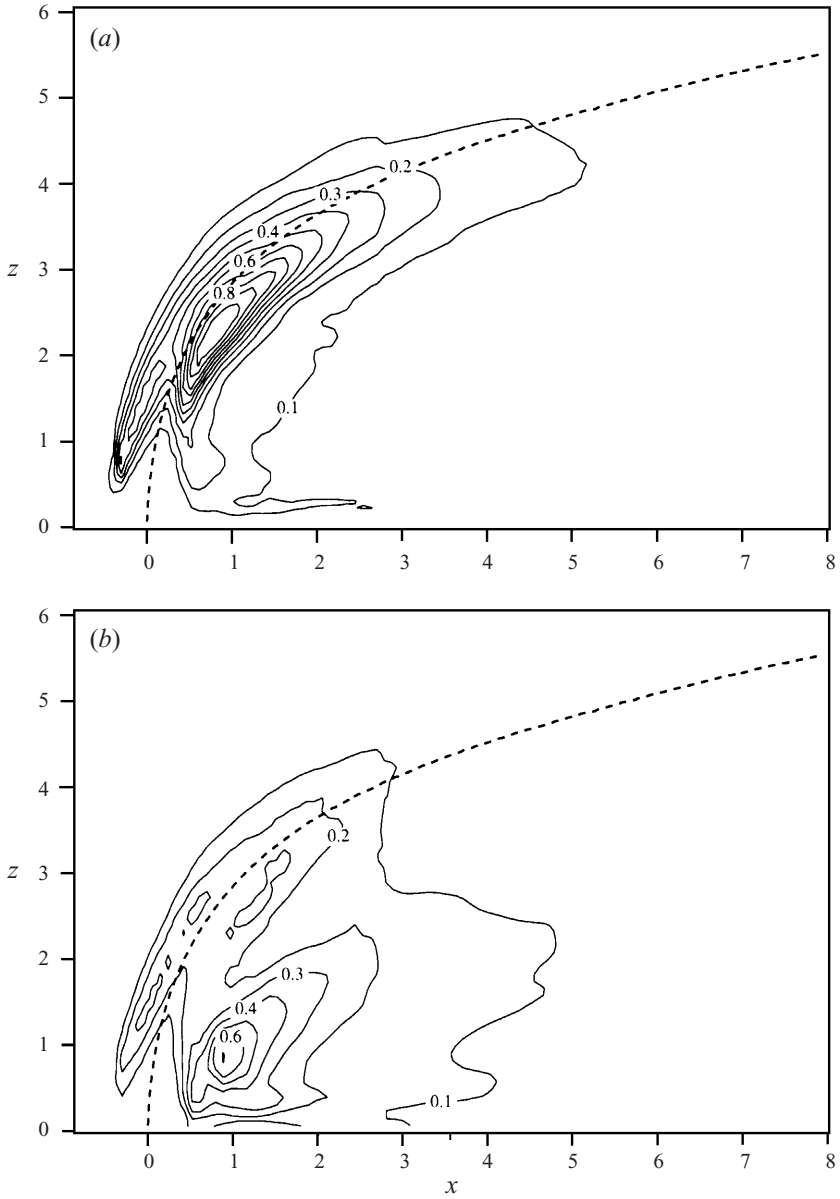

FIGURE 25(*a*, *b*). For caption see facing page.

Because this flow is inhomogeneous in all three directions, the Reynolds stress tensor contains six independent components. For conciseness, we look only at statistics on the centreplane, where symmetry considerations prescribe that two components, $\langle u''v'' \rangle$ and $\langle v''w'' \rangle$, are zero. The remaining four independent elements of the Reynolds stress are plotted in figure 25.

We compare the fluctuations in each of the coordinate directions by looking at figures 25(*a*), 25(*b*), and 25(*c*). The maximum of the TKE above the jet exit observed in figure 23 is composed primarily of u'' and w'' components. The v'' contribution at this point is only half that of the other two components, reinforcing the hypothesis that the turbulence over the jet is generated mainly by spanwise vortical structures.

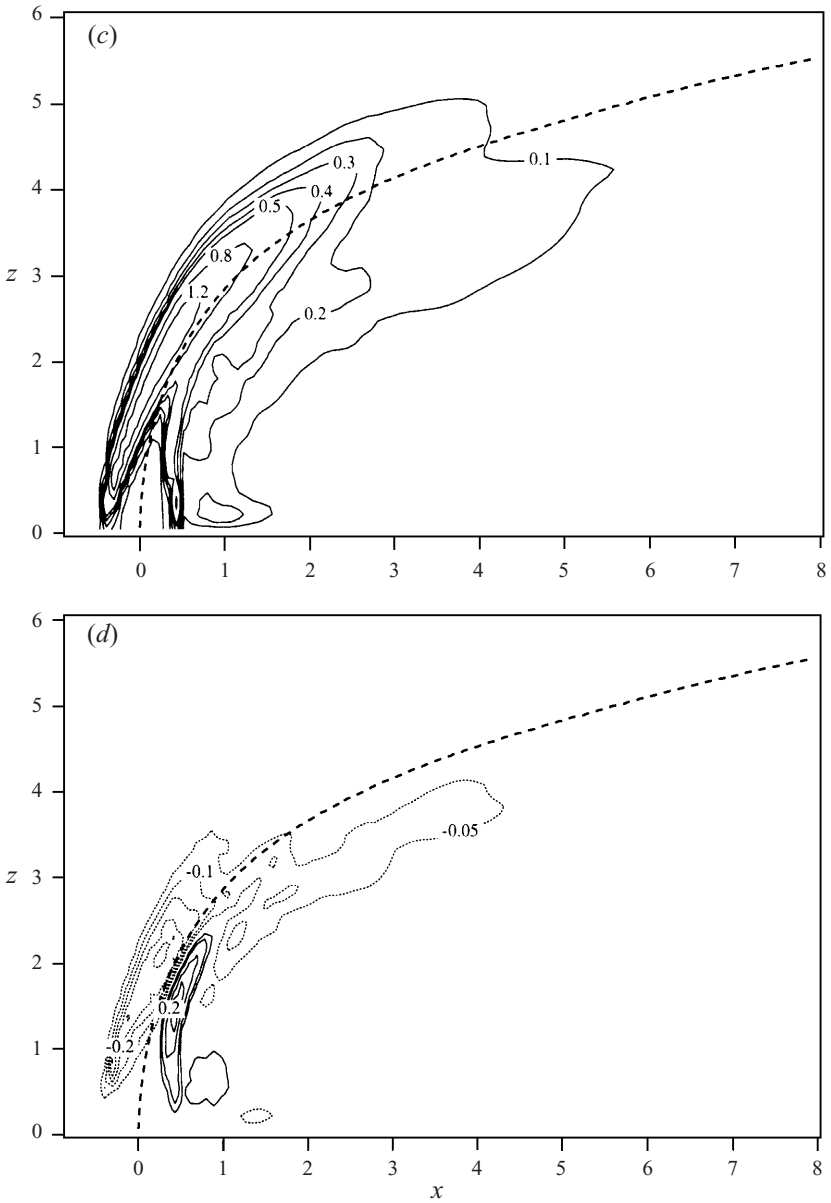

FIGURE 25. Contours of (*a*) $\langle u''^2 \rangle$, (*b*) $\langle v''^2 \rangle$, (*c*) $\langle w''^2 \rangle$ and (*d*) $\langle u''w'' \rangle$ at the centreplane. Contour values as marked. Dotted contours indicate negative values.

Fluctuations in the vertical direction, $\langle w''^2 \rangle$, are concentrated where the spanwise rollers are found (figure 25*c*). The upstream roller produces stronger fluctuations because it rolls up earlier and more regularly. After the rollers meet, fluctuations are biased toward the upstream edge of the jet. Downstream, we observe two distinct branches in the $\langle w''^2 \rangle$ contours, which are most evident in the 0.1 and 0.2 contour lines. The upper branch is the downstream continuation of the fluctuations produced by the spanwise rollers. The lower branch is just below the mean trajectory and is produced by shear between the jet and the crossflow and by the intermittency of the CVP.

Fluctuations in the streamwise direction are small in the pipe flow beneath the flat plate, so we see little sign of $\langle u''^2 \rangle$ until $z \approx 0.5D$. Here, the roll-up of the jet shear layers begins to produce streamwise fluctuations. The location of the $\langle u''^2 \rangle$ maximum lies about $0.5D$ below the $\langle w''^2 \rangle$ maximum, and the maximum $\langle u''^2 \rangle$ magnitude is approximately 60 % that of $\langle w''^2 \rangle$. The lower values of $\langle u''^2 \rangle$ are expected as the initial momentum supplied by the jet is only in the vertical direction.

Regions of high $\langle v''^2 \rangle$ (figure 25 *b*) are located predominantly in the region directly behind the jet, and are due to wake vortices. Above the jet, the magnitude of $\langle v''^2 \rangle$ is not as high as the other two components, but is still significant. These regions of $\langle v''^2 \rangle$ are the signatures of the vertical streaks which form from the spanwise rollers.

The contour plot of $\langle u''w'' \rangle$ (figure 25 *d*) again shows the dominant role played by the spanwise rollers in the near field. $\langle u''w'' \rangle$ is strongly negative in the upstream layer and positive in the downstream one where strong horizontal gradients of the vertical velocity are located. These shear stresses arise from u'' fluctuations and large values of $\partial W/\partial x$ in the upstream and downstream rollers. Similar to the behaviour of $\langle w''^2 \rangle$, the mechanisms by which $\langle u''w'' \rangle$ is produced shifts as the jet turns into the crossflow. Here, gradients in the vertical velocity become small, and a new source of $\langle u''w'' \rangle$, emerges, resulting in the third region of elevated values in the contour plot. Here, in contrast to the roller regions, w'' fluctuations act across a strong $\partial U/\partial z$ gradient to produce shear stress.

7. Conclusions

The present simulations of a jet in crossflow have reproduced experimental measurements. The discrepancies between simulation and experiment can be attributed to differences in Re_D and jet inflow conditions. We have found that slight changes in the upstream condition of the pipe flow in experimental investigations can have significant effects upon the mean flow.

We have identified several new structures in the near field of the JICF. The spanwise rollers on the upstream and downstream edges of the jet are created by a K–H instability. These rollers carry intense velocity fluctuations and account for most of the TKE production in the near field. They also penetrate far into the crossflow and define the upper boundary of the jet. Vertical streaks form as small perturbations in the spanwise rollers are stretched by strong gradients in the vertical velocity.

On the lateral edges of the jet, high streamwise velocities in the crossflow combine with the vertical velocity in the jet to create skewed mixing layers. Quasi-stable hanging vortices form in these layers and extend upwards and downstream behind the jet. Axial velocity through the hanging vortices transports vortical fluid from the near-wall boundary layer of the incoming pipe flow to the back side of the jet. There, the hanging vortices encounter a strong compressive stress and break down, leading to the formation of a weak CVP. We find evidence of the CVP in instantaneous realizations of the flow by low-pass filtering the streamwise vorticity.

In the wake of the jet we find streamwise-oriented vortical structures which are closely related to the horseshoe vortices found upstream of the jet. We also find upright vortices which connect the jet body to the wall. These upright vortices form when streamwise vortices near the wall are reoriented by the strain field directly behind the jet.

The authors gratefully acknowledge computer time provided by the Pittsburg Supercomputing Center and the Stanford EFML. The authors are also grateful to the

National Science Foundation for its support under a High Performance Computing and Communication grant (DMS-9318166), and initially of L. Y. under an NSF Graduate Fellowship. The authors are also grateful to Professor J. C. R. Hunt for useful comments and discussion.

REFERENCES

Andreopoulos, J. 1985 On the structure of jets in crossflow. *J. Fluid Mech.* **157**, 163–197.

Andreopoulos, J. & Rodi, W. 1984 Experimental investigation of jets in a crossflow. *J. Fluid Mech.* **138**, 93–127.

Claus, R. W. & Vanka, S. P. 1992 Multigrid calculations of a jet in crossflow. *J. Propulsion Power* **8**, 425–431.

Coehlo, S. L. V. & Hunt, J. C. R. 1989 The dynamics of the near field of strong jets in crossflows. *J. Fluid Mech.* **200**, 95–120.

Crabb, D., Durao, D. F. G. & Whitelaw, J. H. 1981 A round jet normal to a crossflow. *Trans. ASME: J. Fluids Engng* **103**, 142–153.

Demuren, A. O. 1993 Characteristics of three-dimensional turbulent jets in crossflow. *Intl. J. Engng Sci.* **31**, 899–913.

Fric, T. F. & Roshko, A. 1994 Vortical structure in the wake of a transverse jet. *J. Fluid Mech.* **279**, 1–47.

Haven, B. A. 1996 The effect of hole geometry on the near field characteristics of crossflow jets. PhD thesis, Department of Aeronautics and Astronautics, University of Washington, Seattle, WA.

Huq, P. & Dhanak, M. R. 1996 The bifurcation of circular jets in crossflow. *Phys. Fluids* **8**, 754–763.

Jin, G. & Braza, M. 1993 A nonreflecting outlet boundary condition for incompressible Navier–Stokes calculations. *J. Comput. Phys.* **107**, 239–253.

Johansson, B. C. V. 1993 Boundary conditions for open boundaries for the incompressible Navier–Stokes equation. *J. Comput. Phys.* **105**, 233–251.

Jones, W. P. & Wille, M. 1996 Large eddy simulation of a round jet in a cross-flow. In *Engineering Turbulence Modeling and Experiments 3* (ed. W. Rodi & G. Bergeles), pp. 199–208. Elsevier.

Kays, W. M. & Crawford, M. E. 1980 *Convective Heat and Mass Transfer*, 2nd Edn. McGraw-Hill.

Kelso, R. M., Lim, T. T. & Perry, A. E. 1996 An experimental study of round jets in cross-flow. *J. Fluid Mech.* **306**, 111–144.

Kelso, R. M. & Smits, A. J. 1995 Horseshoe vortex systems resulting from the interaction between a laminar boundary layer and a transverse jet. *Phys. Fluids* **7**, 153–158.

Kim, S. W. & Benson, T. J. 1992 Calculation of a circular jet in crossflow with a multiple-time-scale turbulence model. *Intl J. Heat Mass Transfer* **35**, 2357–2365.

Krauss, T. P., Shure, L. & Little, J. N. 1994 *Signal Processing Toolbox, For Use with MATLAB.* The MathWorks, Inc., Natick, MA.

Lu, G. 1995 A numerical investigation of skewed mixing layers. PhD thesis, Department of Mechanical Engineering, Stanford University, Stanford, CA.

Margason, R. J. 1993 Fifty years of jet in crossflow research. In *Computational and Experimental Assessment of Jets in Cross Flow. AGARD-CP*-534, Winchester, UK.

Moser, R. D. & Rogers, M. M. 1993 The three-dimensional evolution of a plane mixing layer: pairing and transition to turbulence. *J. Fluid Mech.* **247**, 275–320.

Pratte, B. P. & Baines, W. D. 1967 Profiles of the round turbulent jet in a cross flow. *J. Hydraul. Div. ASCE* **6**, 53–63.

Ramsey, J. W. & Goldstein, R. J. 1970 Interaction of a heated jet with a deflecting stream. *NASA Rep.* HTL TR No. 92. NASA Lewis Research Center, Cleveland, OH.

Rudman, M. 1994 Numerical simulation of a jet in a crossflow. In *Intl Colloq. on Jets, Wakes and Shear Layers*, Melbourne, AU. CSIRO.

Salvetti, M. V., Zang, Y., Street, R. L. & Banerjee, S. 1997 Large-eddy simulation of free-surface decaying turbulence with dynamic subgrid-scale models. *Phys. Fluids* **9**, 2405–2419.

Sherif, S. A. & Pletcher, R. H. 1989 Measurements of the flow and turbulence characteristics of round jets in crossflow. *Trans. ASME: J. Fluids Engng* **111**, 165–171 (referred to herein as SP).

Smith, S. H. & Mungal, M. G. 1998 Mixing, structure, and scaling of the jet in crossflow. *J. Fluid Mech.* **357**, 83–122.

Sykes, R. I., Lewellen, W. S. & Parker, S. F. 1986 On the vorticity dynamics of a turbulent jet in a crossflow. *J. Fluid Mech.* **168**, 393–413.

Yuan, L. L. 1997 Large eddy simulations of a jet in crossflow. PhD thesis, Department of Mechanical Engineering, Stanford University, Stanford, CA.

Yuan, L. L. & Street, R. L. 1996 Large eddy simulation of a jet in crossflow. In *Proc. ASME Fluids Engineering Division*, Atlanta, GA. vol. FED 242, pp. 253–260. ASME.

Yuan, L. L. & Street, R. L. 1997 Using domain decomposition with co-located finite volume methods: Two problems and two solutions. In *Proc. ASME Fluids Engineering Division Summer Meeting*, Vancouver, BC, vol. FED SM 97-3645, pp. 1–8. ASME.

Zang, Y. & Street, R. L. 1995 *a* Numerical simulation of coastal upwelling and interfacial instability of a rotating and stratified fluid. *J. Fluid Mech.* **305**, 47–75.

Zang, Y. & Street, R. L. 1995 *b* A composite multigrid method for calculating unsteady incompressible flows in geometrically complex domains. *Intl J. Numer. Meth. Fluids* **20**, 341–361.

Zang, Y., Street, R. L. & Koseff, J. R. 1993 A dynamic mixed subgrid-scale model and its application to a turbulent recirculating flow. *Phys. Fluids* **5**, 3186–3196.

Zang, Y., Street, R. L. & Koseff, J. R. 1994 A non-staggered grid, fractional step method for time-dependent incompressible Navier–Stokes equation in curvilinear coordinates. *J. Comput. Phys.* **114**, 18–33.